UNIVERSITY OF CALIFORNIA

Los Angeles

Low-Cost and Low-Power Phased Array Architectures for Wireless Communication and Sensing

A dissertation submitted in partial satisfaction
of the requirements for the degree
Doctor of Philosophy in Electrical and Computer Engineering

by

Mohammadali Panahi

2023

ABSTRACT OF THE DISSERTATION

Low-Cost and Low-Power Phased Array Architectures
for Wireless Communication and Sensing

by

Mohammadali Panahi
Doctor of Philosophy in Electrical and Computer Engineering
University of California, Los Angeles, 2023
Professor Yuanxun Wang, Chair

This dissertation introduces new approaches for designing a low-cost, low-power, low-noise, and highly linear phased array system for commercial wireless applications. The first approach presents a novel liquid crystal (LC) technology-based structure to reduce the cost, power, and weight of the phase shifter, a critical component in the phased array. LCs, controllable dielectrics with low power consumption, low loss, and cost-effectiveness due to their fabrication using conventional Liquid Crystal Display (LCD) manufacturing technology, enable phase shifting through variations in the main microstrip line's phase constant, loaded periodically with a variable equivalent capacitance controlled by bias voltage. A systematic approach, utilizing transmission line circuit models and periodic structure theory, is developed for efficient design optimization using advanced design system (ADS) and HFSS softwares. The fabricated phase shifter achieves an impressive FOM of $105.9°/dB$.

In the second approach, a modified architecture for a mixer-first phased array receiver is proposed, addressing the demand for high linearity and low noise in commercial wireless applications. Instead of conventional low-noise-amplifiers (LNAs), a new time-variant transmission line (TVTL) mixer serves as the initial stage, showcasing exceptional performance with a broadband conversion gain of up to 4.2 dB, a low noise figure of 3 dB, and an input-referred P1dB of 12 dBm. Addition-

ally, a low-cost, low-power LC phase shifter is integrated into the LO-path, minimizing the impact of lossy phase shifters on receiver noise figures.

Finally, the third approach proposes a novel analog beamforming architecture for a low-cost, low-loss, and power-efficient dual-beam phased array system, highly desirable for commercial wireless and satellite applications. This system generates multiple concurrent, independent directive beams with high gain, enabling a terminal to track and connect to multiple base stations, facilitating flexible and broad coverage multipoint communications with improved signal-to-noise ratios. The proposed architecture employs sub-arrays of two antenna elements fed by an orthogonal two-port signal combiner consisting of a 90-degree hybrid block. Each sub-array generates two orthogonal beams, driven by a phase shifter, allowing for the formation of two sharper overall beams and fine, independent scanning within each sub-array beam. Additionally, an optimal antenna array column shift method is proposed to reduce the high side lobes introduced by sub-array usage. Phased array pattern measurements exhibit continuous beam scanning over elevation angles of 0° to 45° degrees and azimuth angles of 0° to 20° degrees for both right and left beams, with a maximum gain of 20.8 dBi and Side-lobe Level (SLL) of -13.7 dB.

The dissertation of Mohammadali Panahi is approved.

Danijela Cabric

Aydin Babakhani

Gregory J. Pottie

Yuanxun Wang, Committee Chair

University of California, Los Angeles

2023

TO GOD AND MY FAMILY, GRATEFUL FOR UNWAVERING SUPPORT

TABLE OF CONTENTS

LIST OF TABLES

LIST OF FIGURES

Symbols and Acronyms

PA	Power Amplifier
LCPS	Liquid Crystal Phase Shifter
TVTL	Time-varying Transmission Line
NF	Noise Figure
LNA	Low Noise Amplifier
FOM	Figure Of Merit
MEMS	Micro-Electromechanical System
RTPS	Reflection-Type Phase Shifter
LTPS	Loaded-Transmission Line Phase Shifter
STPS	Switched-Type Phase Shifter
STPS	Switched-Type Phase Shifter
AR	Axial Ratio
ABF	Analog Beamformer Network
ABF	Analog Beamformer Network

ACKNOWLEDGEMENTS

During my PhD journey at UCLA, I had the privilege of meeting numerous amazing and inspiring individuals, from whom I learned invaluable lessons. I am deeply grateful to all of them for their help and support.

First and foremost, I extend my sincere gratitude to my advisor, Professor Yuanxun Wang, whose guidance and unwavering support throughout my Ph.D. program have been invaluable. His patience and dedication have been a tremendous source of strength during challenging times in my research.

I would also like to thank my committee members, Prof. Aydin Babakhani, Prof. Danijela Cabric, and Prof. Greg Pottie, for their technical support during my studies. My sincere thanks go to the distinguished UCLA faculty members, especially Professor Yahya Rahmat-Samii, Professor Behzad Razavi, and Professor Tatsuo Itoh, for their mentorship and wisdom.

My heartfelt appreciation goes to the staff of the electrical and computer engineering department, including Deeona Columbia, Katie Christensen, and Celina Liebmann, for their assistance during my PhD journey.

In the lab, I owe a debt of gratitude to my labmates, especially Maziar Hedayati, Foad Freidoony, Lap Yeung, Kamal Bhakta, Xianting Zouand and Gabriel Morozowsky, whose endless discussions and collaboration have contributed to the excellence of this work.

To my dear friends, including Javad Ebrahimizadeh, Christopher Chen, Mehrdad Babmir, Hossein Razavi, Iman Habibagahi, Manie Tadayon, Hamed Nilchi, Behzad Ashrafi and Alireza Asadi, I thank you for your unwavering support and cherished memories.

To my family, I am forever grateful to my parents and my brothers Maysam and Amirhossein. A special thank you to my mother for her unwavering emotional support throughout my life. You will always be my role model.

Lastly, I express my gratitude to my God for his grace and guidance in every step of my journey.

VITA

EDUCATION

2018-2023 **PhD candidate in Electrical and Computer Engineering**,
University of California, Los Angeles, USA

PUBLICATIONS

Chapter 1

INTRODUCTION

A phased array antenna is a sophisticated multiple-antenna system with the remarkable ability to enhance the radiation pattern in a specific direction while suppressing radiation in undesired directions. This unique capability allows for electronic steering of the antenna's radiation, eliminating the need for mechanical rotation mechanisms. Since its inception, the concept of phased arrays has been a groundbreaking development, enabling a diverse range of applications to benefit from its advantages.

Engineers and researchers have harnessed the power of this innovative system to achieve precise control over the directionality of the antenna. As a result, phased array antennas have become valuable tools in various fields, including telecommunications, radar systems, satellite communications, and more. The widespread use of phased arrays has revolutionized the design and implementation of wireless communication systems, offering enhanced performance and adaptability in modern communication networks. This chapter will explore numerous potential applications that can capitalize on the benefits of phased array technology.

However, despite their significant advantages, the widespread adoption of phased array systems in large-scale commercial applications faces obstacles primarily due to their high cost and complexity. Overcoming this challenge necessitates a substantial reduction in the cost and complexity of these antennas to make them more accessible for diverse commercial uses. To address this, ongoing efforts are dedicated to developing new architectures that effectively lower the complexity of phased array systems. The goal is to create low-cost, low-power solutions that can unlock the full potential of phased array technology across various industries and services. This thesis presents an overview of several new approaches and architectures aimed at designing and implementing such

low-cost and low-power phased arrays.

1.1 Phased Array Background and Application

Phased arrays have a rich history of application in radar systems, where they have been used for several decades. Radar systems, whether based on continuous wave or pulsed signals, rely on emitting and collecting signals in a specific direction to process and extract information for object identification. Phased array radars offer a versatile solution, allowing a single radar system to perform surface detection and tracking as well as air detection and tracking. The electronic beam steering capability of phased array radars far surpasses traditional radars using mechanical rotation, providing significantly faster response times.

In the realm of telecommunications, phased arrays find extensive use in base stations to enhance signal coverage in specific areas while minimizing interference in others. The technology is also employed in satellite TV systems, where phased array-based broadcasting-reception links outperform traditional parabolic dish systems. These advantages include improved robustness in inclement weather, smaller profile, and lower weight, making them easier to mount on walls and roofs. The adaptive beamforming capability further enables mobile objects such as planes and vehicles to access satellite programs.

Phased arrays have also found emerging applications in the biomedical field. In microwave imaging, phased arrays are utilized to detect early-stage breast cancer. The method involves emitting wideband impulses from an antenna array placed on the breast surface. The receiver uses beamforming techniques to focus on the backscattered signal from malignant tumors and compensate for frequency-dependent propagation effects. Microwave imaging offers higher detection probabilities compared to X-rays or ultrasound, thanks to the significant contrast provided by the dielectric discontinuity caused by malignant tumors. Moreover, microwave imaging is a more cost-effective and less harmful alternative to magnetic resonance imaging (MRI) and X-rays.

The phased array application is shown in Figure 1.1. The versatile capabilities of phased array systems have made them instrumental in various fields, ranging from radar technology and

telecommunications to biomedical applications, paving the way for improved performance, adaptability, and innovative solutions in each domain.

Figure 1.1: Phased array application.

1.2 Phased Array Principle

The principle of the phased array is depicted in Figure 1.2. It involves controlling the phase shift of each element within the array to achieve beam steering and beamforming. The mathematical representation of the phased array principle is commonly expressed using complex phasors. The steered beam of the array follows the relation:

$$\Delta\phi(\omega) + k_0 \times d \times \cos(\theta(\omega)) = 0 \tag{1.1}$$

where $\theta(\omega)$ is the frequency-dependent beam angle, and k_0 is the wavenumber at central operational frequency, d represents the separation distance of array elements, and $\Delta\phi(\omega)$ is the phase shift through the phase shifter. The array factor for an odd n-element array is calculated by:

$$AF = 2\frac{\sin(\frac{(n-1)\Delta\phi(\omega)}{4})}{\sin(\frac{(\Delta\phi(\omega))}{2})} \tag{1.2}$$

which shows that the gain of the array is equal to the conventional series fed N-element array, however. the Half-Power-Beam-Width (HPBW) is increased.

Phased arrays offer significant advantages in extending the maximum range of reliable communication between transmitting and receiving systems. The distance over which reliable communication can occur depends on the maximum power transmitted in the receiver's direction. By implementing transmitter antennas using phased arrays, it becomes possible to boost the transmit power in the desired direction while keeping the total power transmitted the same. This allows phased array transmitters to communicate over longer distances compared to omnidirectional transmitters for a given receiver sensitivity. Unlike omnidirectional transmitters that waste a major fraction of radiated power and cause interference for other users, phased array transmitters focus their power in specific directions, minimizing waste and interference, making them more efficient in congested wireless environments.

In a receiver based on using phased arrays, the signals at the output of the array are combined coherently to receive signals from the desired direction. The coherent combination of currents from the antenna elements results in an output current that is n times larger than the current at each individual antenna, leading to a signal power level at the output that is n^2 times larger than the received signal. However, the noise from the receive channels is not coherent, and at the output of the phased array, the power of noise from different channels gets combined. Consequently, the output noise level becomes n times larger than the noise contribution of each channel n. As a result, the noise figure of the entire system can be calculated as shown in equation 1.3. This coherent signal combining in phased arrays provides significant signal power gain, but it also amplifies the noise, which needs to be carefully managed in system design.

$$NF_{\text{Phased Array}} = \frac{nP_N}{n^2 P_S} = \frac{NF_{\text{channel}}}{n} \tag{1.3}$$

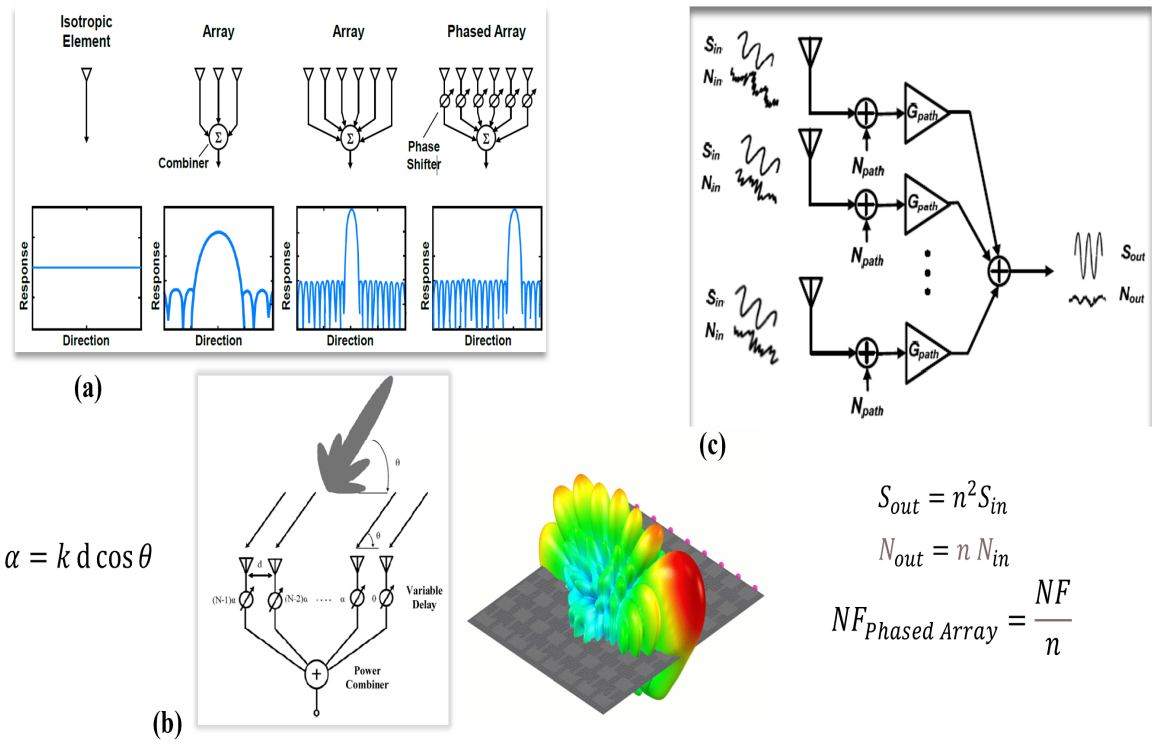

Figure 1.2: Phased array principle.

1.3 Phased Array Architecture

Figure 1.3 illustrates the various phased array architectures based on the placement of phase shifters. Phase shifters can be positioned at different stages of the phased array system, leading to four distinct types: RF-phase shifting, LO-phase shifting, IF-phase shifting, and digital phased arrays. In the upcoming sections, each of these phased array types will be discussed in detail.

In the RF phase-shifting architecture, signals from antenna elements undergo phase shifting and RF domain combination before being down-converted to baseband through heterodyne or homodyne mixing. This approach is traditionally more prevalent in phased array design due to its compactness and simplified LO signal distribution, requiring only one mixer. Additionally, it offers better interference insulation from undesired directions and filters out interferers at the RF stage before down-conversion, reducing the stringent requirements on the mixer's dynamic range. However, implementing high-performance RF phase-shifters operating at RF frequencies poses a challenge, as passive phase shifters exhibit microwave and millimeter regime losses, while

active phase shifters suffer from low dynamic range, crucial for operation in the presence of strong interferers.

The general architecture of phased arrays based on LO (Local Oscillator) phase shifting involves manipulating the LO signal's phase to indirectly change the RF (Radio Frequency) signals' phases at each channel. This approach offers advantages over other architectures that use phase shifters on the signal path. By tuning the LO signal's phase, the RF signal's phase can be controlled without the need for phase shifters on the signal path. This avoids direct impacts of phase shifter losses, nonlinearity, and noise on the overall system performance. However, this method requires a large number of mixers, leading to higher system complexity and power consumption compared to phased arrays using RF stage phase shifting. The choice between LO phase shifting and RF phase shifting depends on application-specific requirements, considering trade-offs in simplicity, performance, and power consumption.

The general architecture of phased arrays based on IF (Intermediate Frequency) phase shifting involves tuning the IF signal's phase, thereby determining the RF (Radio Frequency) signal's phase at each channel. This method offers advantages over RF and LO phase shifting as it operates at lower frequencies, allowing for better-performing phase shifters along the IF path, leading to improved loss, nonlinearity, and noise performance. However, a considerable number of mixers are still needed, contributing to system complexity and power consumption. Additionally, interference cancellation occurs only after the IF stage, necessitating highly linear mixers to effectively handle strong interference from undesired directions. The choice between IF phase shifting, RF phase shifting, and LO phase shifting depends on specific application requirements, carefully considering the trade-offs between performance, complexity, and power consumption.

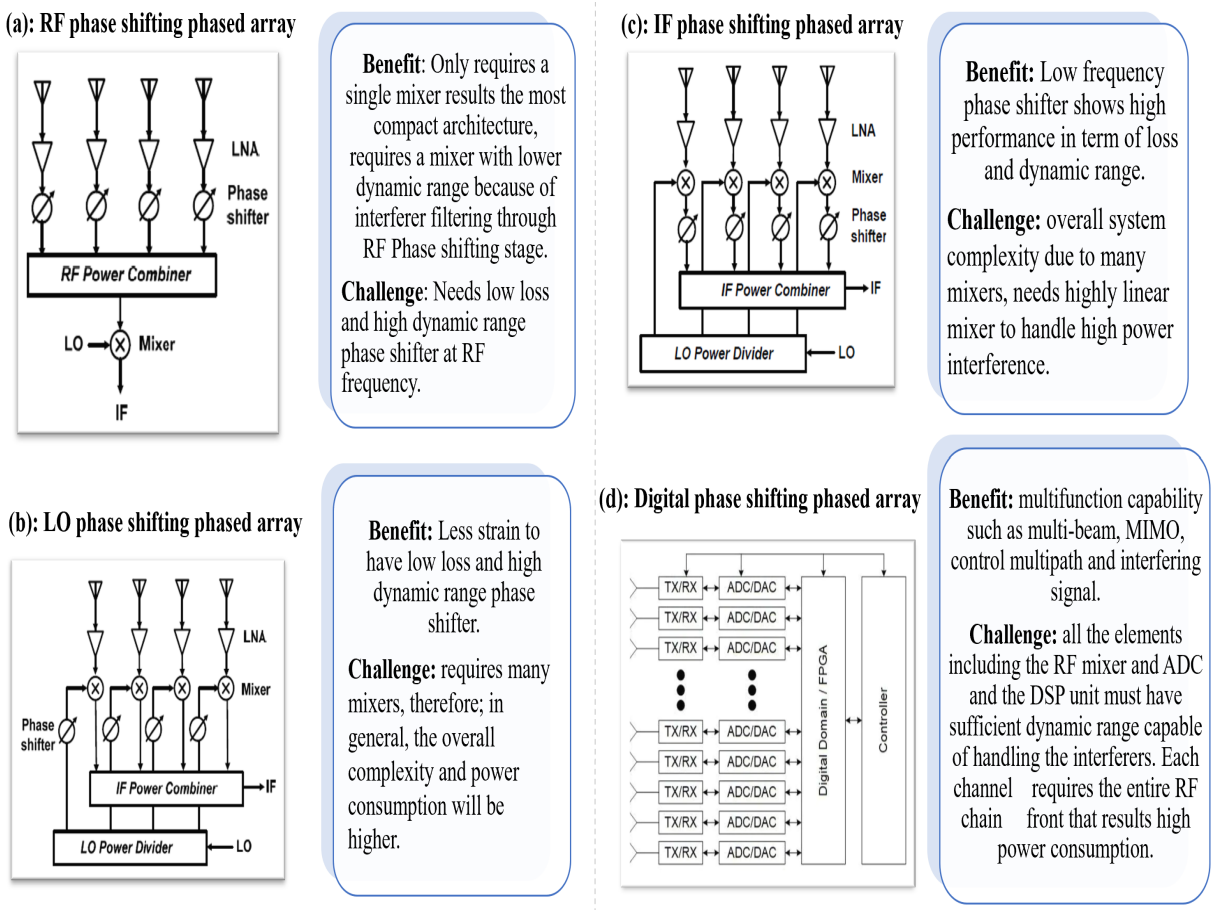

Figure 1.3: Phased array architectures.

1.4 Phase Shifter Topology

Phased arrays have been traditionally used in defense applications for several decades. However, there are still major constraints against using them in commercial applications, and these include their high cost, power consumption, and high hardware complexity. To use the phased array in commercial applications, there is a need for low-cost, low-power, and low-weight tunable phase-shifters as a key component. To compare their electrical performance, the classical figure of merit (FOM) [1] is used as the ratio of the maximum differential phase shift and the maximum insertion loss.

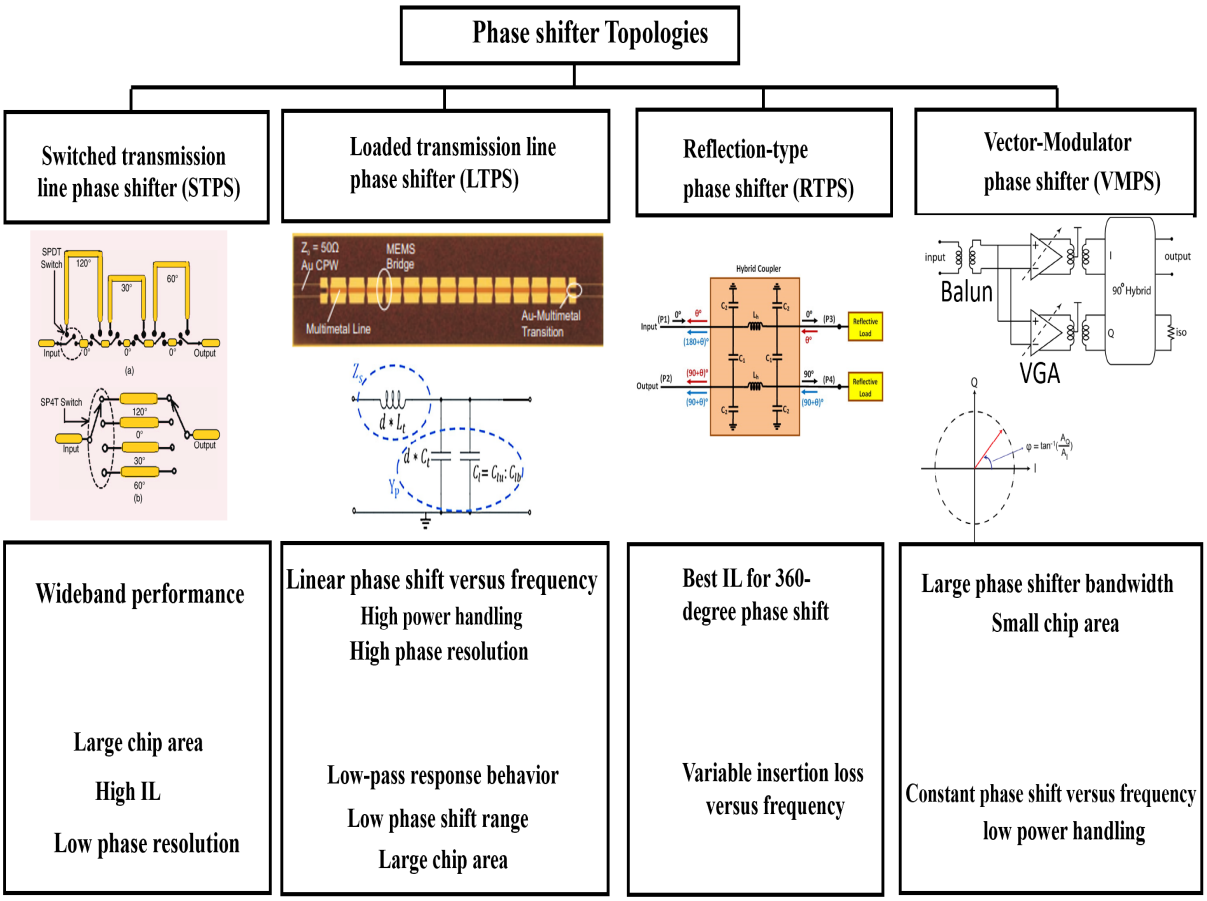

Figure 1.4: Phase shifter topologies.

The phase shifter topologies are shown in Figure 1.4. Phase shifters can be classified into two categories: active and passive [2]-[3]. Active phase shifters provide gain while having more power consumption and introducing more non-linearity to the system. Vector modulators (VMs) are one of the most common active phase shifters, used in applications that do not require high resolution and high dynamic range. In the vector modulator structure, the input signal is divided by two signals with a quadrature phase in a quadrature generator (QG). Then, the amplitude of each signal is scaled with variable gain amplifier (VGA), and finally, a combiner adds two signals to achieve the desired phase shift [4]. Passive phase shifters can achieve more power handling for large input signal with lower power consumption but exhibit higher insertion loss. To achieve a low insertion loss, an optimized phase shifter topology can be implemented by different technologies of CMOS, BiCMOS, Barium Strontium Titanate (BST), Liquid Crystal, and micro-electromechanical

system (MEMS). Three conventional topologies are considered to design passive phase shifters, which are reflection-type phase shifter (RTPS), loaded transmission line phase shifter (LTPS), and switched transmission line phase shifter (STPS) [2]-[3]. The RTPS is based on a 90° hybrid coupler connected to a load, like a varactor diode, which is varying continuously to create the phase shift. In [5], a new switched inductor load structure is proposed to have a simple and low power control voltage block in the RTPS with an average insertion loss of 9.5 dB at 29 GHz. RTPS can achieve high resolution; however, varactor quality factor, Q, and loss vary across capacitance settings, leading to insertion loss variation with the phase shift. This loss variation results in a nonuniform amplitude distribution in phased array antennas and increases the side-lobe-level (SLL). The LTPS topology is based on a transmission line loaded periodically with shunt or series loads, which are tuned to obtain a phase shift. A transmission line loaded periodically with MEMS bridge is proposed in [6], and a FOM of $150^\circ dB$ was achieved. MEMS may need expensive packaging to protect the movable MEMS bridges against the environment. In the STPS, the RF signal propagation length is switched between delay lines of different physical lengths, which is implemented with p-i-n diode, MOS-FET, or MEMS switches. By using an improved switching time CMOS transistor, a low loss STPS was achieved in [7]. A drawback of the STPS is phase resolution limitation, generated by the number of transmission lines and switches, which is in trade-off with the insertion loss. Another way to make phase shifters based on transmission lines is to use materials with controllable permittivity and permeability, like ferroelectric or ferrite, as a substrate. A phase shifter implemented with a GCPW line under barium strontium titanate (BLT) accomplished a high FOM of 221.4° dB [8]. Even though these materials lead to high FOM phase shifters, they need a high driving voltage or power and high fabrication costs.

1.5 Overview of Thesis

This thesis introduces new phase shifter and phased array architectures aimed at reducing power consumption, cost, and complexity in wireless communication applications. In the second chapter, a novel structure based on liquid crystal (LC) technology is presented, achieving a high figure of

merit (FOM) phase shifter operating at sub-6 GHz frequencies. The phase-shifting mechanism relies on phase constant variation in the main microstrip line, periodically loaded by a variable equivalent capacitance controlled through a bias voltage. A systematic design optimization approach, based on a transmission line circuit model and periodic structure theory, is developed using ADS and $HFSS$ software. The fabricated phase shifter demonstrates an impressive FOM of $105.9°dB$, reaching a maximum insertion loss of 4.35 dB, and providing a maximum phase-shift of $461°$ at 4 GHz, covering the sub-6 GHz 5G band.

In the third chapter, a modified architecture for a mixer-first phased array receiver is proposed, addressing the need for high linearity and low noise in commercial wireless applications. Replacing the conventional LNA, a new time-variant transmission line (TVTL) mixer serves as the initial stage. The MMIC TVTL chip exhibits excellent performance with up to 4.2 dB broadband conversion gain, a low noise figure of 3 dB, and an input-referred P1dB of 12 dBm. Additionally, a low-cost and low-power LC phase shifter is integrated into the LO-path, minimizing the impact of lossy phase shifters on the receiver's noise figure.

Chapter four presents a novel analog beamforming architecture for a low-cost, low-loss, and power-efficient dual-beam phased array system, ideal for commercial wireless and satellite applications. This system generates multiple concurrent and independent directive beams with high gain, allowing a terminal to track and connect to multiple base stations, enabling flexible and broad coverage multipoint communications with superior signal-to-noise ratio. The proposed architecture utilizes sub-arrays of two antenna elements fed by an orthogonal two-port signal combiner consisting of a 90-degree hybrid block. Each sub-array generates two orthogonal beams, driven by a phase shifter enabling the formation of two sharper overall beams and fine, independent scanning within each sub-array beam. Additionally, the chapter introduces the optimal antenna array column shift method to reduce high side lobes typically introduced by sub-array usage.

Finally, the last chapter concludes the thesis and highlights its main achievements.

Chapter 2

SUB-6 GHZ HIGH FOM LIQUID CRYSTAL PHASE SHIFTER FOR PHASED ARRAY ANTENNA

2.1 Introduction

Fifth-Generation mobile communication is just around the corner to provide high data-rate and system capacity by using a combination of sub 6- GHz and millimeter-wave frequencies [9]-[10]. To achieve a higher gain and better signal coverage in 5G mobile communication, advanced phased array or multi-beam antenna systems have been developed [11]-[12].

To use the phased array in commercial applications, there is a need for low-cost, low-power, and low-weight tunable phase-shifters as a key component. The performance of different phase shifters is summarized further in Table 2.3. To compare their electrical performance, the classical figure of merit (FOM) [1] is used as the ratio of the maximum differential phase shift and the maximum insertion loss, as given in equation 2.1.

$$FOM = \frac{\triangle\phi_{max}}{IL_{max}} \tag{2.1}$$

Liquid crystals are controllable dielectrics which demonstrate large electrically controlled birefringence in the microwave frequency domains. They are planar in shape, low power, low loss and especially low cost because they are fabricated using the conventional Liquid Crystal Display (LCD) manufacturing technology. Nematic LCs [13] are a type of tunable anisotropic dielectric whose properties could be controlled by using surface anchoring, or an external electric or magnetic fields. Nematic LCs possess relatively low dielectric loss in the microwave frequency range,

require low operation voltage, and have continuous tuning ability. They have become more and more widely used in various microwave applications, such as phase shifters [14]-[18].

There are various designs for LC-based phase shifters, mostly in millimeter-wave frequencies. A 2-D phased-array antenna with LC-based variable delay lines is presented in [19], and the FOM achieved was $62.5^{\circ}/dB$ at 17.5 GHz. A tunable liquid crystal phase shifter based on periodically loaded CPW transmission line is proposed in [20], and the FOM achieved was $60^{\circ}/dB$ at 20 GHz. The dielectric loss tangent of LC material decreases with an increasing frequency, and LC's generally exhibit their highest performance at frequencies above 10 GHz [21]. This is the reason that most LC-based phased shifters have been proposed in the millimeter-wave frequencies; that way, they achieve higher FOM. Even though many topologies have been well developed at millimeter-wave frequencies, they suffer from RF loss in the frequencies lower than 10 GHz. Thus, to design a LC-based phase shifter at low frequencies, a new topology is still necessary to reach a high FOM in sub-6 GHz applications.

In this chapter, a novel structure for LC-based phase shifter (LCPS) is proposed, which achieves an FOM of $105.9^{\circ}/dB$ at 4 GHz while the insertion loss is roughly constant over the operational bandwidth. In the previous LTPS [20], the main transmission line, with a characteristic impedance higher than 50 Ω, is loaded directly with a shunt capacitance by using one tuning stub. In the proposed novel structure for LCPS, the lower than 50 Ω microstrip line is used to have a bigger line width and lower ohmic loss, while the 50 input matching is implemented with a tapered transmission line. To increase the phase shift in the proposed LCPS, the main low impedance transmission line is periodically loaded with an equivalent capacitance created with two series tuning stubs. These two stubs allow us to achieve a higher loaded capacitance compared with the directly loading shunt capacitance with one tuning stub [20], resulting a higher FOM.

2.2 LC Phase Shifter Theory, Design And Measurement

2.2.1 Microstrip Line LCPS structure

The proposed Microstrip line LC-based phase shifter (MLCPS) is shown in Figure 2.1. The phase shifter structure is implemented by two glass layers as a substrate with thickness of h_G, and a Nematic liquid crystal as a tunable dielectric is contained between them with a fixed thickness of h_{LC}. As shown in Figure 2.1a, the MLCPS is a two-port component, which consists of a main microstrip transmission line loaded with a shunt stub, creating a periodic structure with 80 unit-cells to reach 360° phase-shift. To match the input impedance of the periodic structure to 50 Ω, a microstrip line transition is used at the MLCPS input and output. The MLCPS unit-cell with specified dimensions is shown from top view in Figure 2.1b, and from the cross section in Figure 2.1c. Each unit-cell consists of a copper-based main microstrip line deposited on the top-surface of glass$_1$, and a copper-based microstrip ground implemented on bottom-surface of glass$_1$. The microstrip line width and thickness is defined with W_m and t respectively. In each unit-cell, the main microstrip line is connected to the red-colored microstrip line stub, which is specified with the dimension of (t, W_s, l_s) in the direction of X, Y, and Z respectively. A green pad shown in Figure 2.1b with the dimension of $a * b$, is connected to the red-colored stub on the top-surface of glass$_1$. This green pad has an intersection with the microstrip line G-stub deposited on the bottom-surface of glass$_2$, making an LC-based parallel-plate capacitance like a bridge, as shown in Figure 2.1c with a dash line. The G-stub is used to connect the LC parallel-plate capacitance to the main microstrip ground by using a soldered ground connection implemented on the edge of glass$_1$. The G-stub has a width W_{GS}, a length l_{GS} and a thickness t. The length of each unit-cell P is a periodic spacing in MLCPS structure.

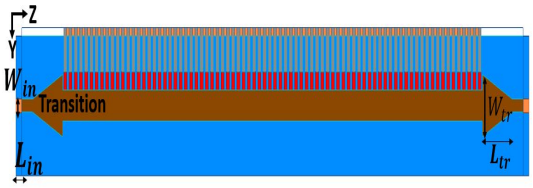

(a) 80 unit-cells with impedance matching transition top-side view

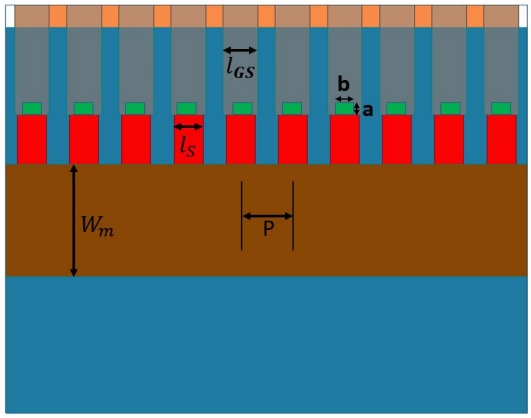

(b) 10 unit-cells top-side view

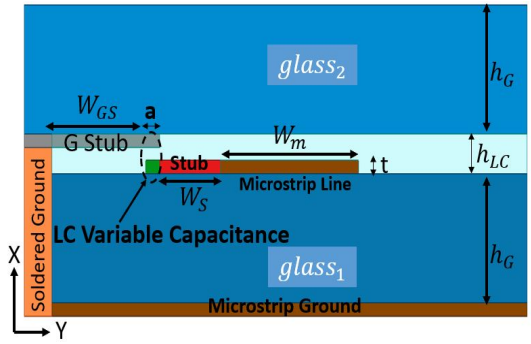

(c) Cross-side view

Figure 2.1: Proposed Microstrip line LCPS structure constructed by a microstrip line periodically loaded by a variable equivalence capacitance.

Figure 2.2 describes the usage of LC parallel-plate capacitance, shown with the dash-line in Figure 2.1c, and how to make a variable LC capacitance for phase-shifting mechanism. The LC material sandwiched between two copper plates as an electrode, consists of uniaxial anisotropic molecules [22]. When the external bias voltage between the copper electrodes is zero, the LC molecules are aligned perpendicularly to the RF field, as shown in Figure 2.2a. In this perpen-

dicular case, the effective permittivity ε_{eff} and loss tangent $\tan\delta$ seen by the RF field are equal to $\varepsilon_{r,\perp}$ and $\tan\delta_{\perp}$, respectively. The LC molecules are aligned parallel to the RF field when an external bias voltage that is larger than the saturated voltage V_{sat} is applied between the copper electrodes, as shown in Figure 2.2b. In this parallel case, the effective permittivity ε_{eff} and loss tangent $\tan\delta$ experienced by the RF field are equal to $\varepsilon_{r,\parallel}$ and $\tan\delta_{\parallel}$, respectively. By controlling the external bias voltage applied to the electrodes from 0 to V_{sat}, the effective permittivity of the parallel-plate capacitance is changed from $\varepsilon_{r,\perp}$ to $\varepsilon_{r,\parallel}$ as a function of LC molecules orientation. This mechanism results in a variable capacitance controlled by the external bias voltage. The upper LC capacitance electrode is connected to the main microstrip ground, which is used as the bias voltage ground too. The lower LC capacitance electrode is connected to the main microstrip line. Therefore, to excite the phase shifter with the bias voltage and the RF signal simultaneously, a Bias-Tee microwave component is used to add the external bias voltage to the RF-INPUT. Thus, the variable capacitance controlled by the bias voltage is loaded to the main transmission line and will cause a phase shift in the phase shifter by changing the phase constant.

Figure 2.2: Variable capacitance shown in Figure 2.1c, is created by a sandwiched LC material between two electrodes for applying electric field. The effective permittivity of the LC material is changed from (a) when there is no external bias voltage, to (b) when saturated bias voltage is applied.

2.2.2 Microstrip Line LCPS Theory

To analyze and design the proposed MLCPS, the distributed circuit model is very useful. Each of the MLCPS unit-cell is modeled with transmission lines and is shown in Figure 2.3. The main microstrip transmission line shown with width W_m and length P, in Figure 2.1b, is modeled as a transmission line with a characteristic impedance of Z_0 and an electrical length of θ° at the center frequency of f_0. The red-colored stub and G-stub are modeled as transmission lines with characteristic impedance and electrical lengths of Z_s, ${\theta_s}^\circ$, Z_{GS} and ${\theta_{GS}}^\circ$. The LC variable capacitance is modeled with C_{LC}, which varies from C_{per} to C_{par} when LC molecules rotate from perpendicular case to parallel case. The LC variable capacitance can be loaded directly with one stub to the main transmission line [20]; however, it is loaded indirectly between two stubs like a bridge in each MLCPS unit-cell, as shown in Figure 2.1-2.3. The stubs′ electrical length ${\theta_S}^\circ$, and ${\theta_{GS}}^\circ$, are finally tuned in a way to see roughly capacitive admittance $j\omega_0 C_l$ from the input of loaded stubs. These two stubs allow us to have more flexibility in design, and to reach a bigger equivalent loaded capacitance C_l from LC variable capacitance C_{LC}, resulting in a higher FOM. The unit-cell transmission line model, shown in Figure 2.3, is simplified and modeled with lump-elements in Figure 2.4. The loaded shunt capacitance C_l varies from C_{lu} to C_{lb}, when the bias voltage increased from the minimum to the saturation voltage V_{sat}. The ratio of maximum loaded capacitance to the minimum loaded capacitance C_r is given in equation 2.2. This ratio is a function of parallel to perpendicular case relative permittivity, since the other parameters in the loaded capacitance are constant.

$$C_r = C_{lb}/C_{lu} \cong \varepsilon_{r,\parallel}/\varepsilon_{r,\perp} \tag{2.2}$$

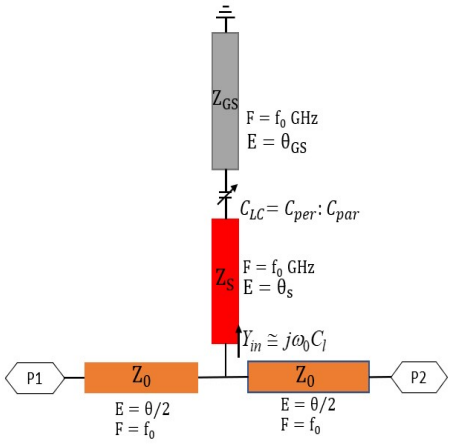

Figure 2.3: Distributed transmission line model of the MLCPS unit-cell, assuming the variable LC capacitance shown in Figure 2.1 and 2.2 can be representative by C_{LC}.

The main microstrip transmission line, defined with Z_0 and θ° in Figure 2.3, is modeled with per unit length inductance L_t and capacitance C_t. The value of L_t and C_t are driven based on the value of Z_0, given by [23]

$$C_t = \frac{\sqrt{\varepsilon_{reff}}}{v_c Z_0} \; and \; L_t = C_t Z_0^2 \tag{2.3}$$

in which ε_{reff} is the effective dielectric constant of the transmission line with the characteristic impedance Z_0, shown in Figure 2.3, and v_c is the free space velocity. The proposed $MLCPS$ is modeled with distributed lump-elements by cascading the unit-cell model represented in Figure 2.4. The input Bloch impedance of this periodically loaded line for the un-biased case is given by [24]-[25].

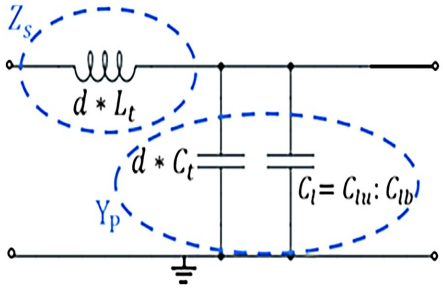

Figure 2.4: Lumped-element transmission line model of the MLCPS unit-cell shown in Figure 2.3, assuming the input admittance shown in Figure 2.3 can be representative by a shunt capacitance C_l.

$$Z_{BU} = \sqrt{\frac{Z_s}{Y_p}}\sqrt{1-\left(\frac{\omega}{\omega_B}\right)^2} = \sqrt{\frac{d^* L_t}{d*C_t + C_{lu}}}\sqrt{1-\left(\frac{\omega}{\omega_B}\right)^2} \tag{2.4}$$

where ω_B is the Bragg frequency and given by [24]-[25]:

$$\omega_B = 2/\sqrt{d*L_t(d*C_t + C_{lb})} \tag{2.5}$$

By using the equations (2.2), (2.4) and (2.5), the periodic length of each unit-cell d, and the un-biased loaded capacitance C_{lu}, is determined and represented by equation (2.6) and (2.7).

$$d = \frac{Z_{BU}}{\pi f_B \sqrt{L_t(C_r L_t - (C_r - 1)C_t {Z_{BU}}^2)}} \tag{2.6}$$

$$C_{lu} = \; d\left(\frac{L_t}{{Z_{BU}}^2} - C_t\right) \tag{2.7}$$

The phase shift per unit length is calculated from the change of phase constant experienced by the external bias voltage [25]:

$$\Delta\phi = \omega\sqrt{L_t C_t}\left(\sqrt{1+\frac{C_{lb}}{d*C_t}} - \sqrt{1+\frac{C_{lu}}{d*C_t}}\right) \tag{2.8}$$

2.2.3 Microstrip Line LCPS Design

To design the phase shifter proposed in Figure 2.1, the primary parameters are defined and shown in Table 3.1. The center frequency of 4 GHz and 50 Ω input-matching with bandwidth of 500 MHz, are aimed to support the 5G applications in Sub-6 GHz channel. A glass material with relative permittivity of 4.8 and loss tangent of 0.007 is used for MLCPS substrate. The external bias is a function of LC material type. The relative permittivity of the used LC material is changed from the perpendicular case ($\varepsilon_{r,\perp}$ =2.7) to the parallel case ($\varepsilon_{r,\parallel}$ =3.77), when the peak-to-peak bias voltage amplitude varies from 2 to 20 V_{p-p}. There is no phase shift response between 0V and 2V, so the measurement is reported from 2 to 20 V_{p-p}. The maximum phase shift is accomplished in MLCPS, when a rectangular pulse with a frequency of 277 Hz is applied as an external bias.

The LC material permittivity response depends on the external bias voltage and frequency. For the LC material used in the proposed LCPS, the biggest phase shift response is achieved in the measurement with the drive frequency of 277 Hz. In the proposed novel structure for LCPS, the main microstrip line, with a characteristic impedance Z_0 lower than 50 Ω, is used to have a bigger line width and lower ohmic loss, improving the FOM.

Table 2.1: The Primary Specified Parameter To Design MLCPS

f_0	4 GHz	h_G	700 μm
f_B	27 GHz	h_{LC}	4 μm
Z_0	28 Ω	$\varepsilon_{r,\parallel}$	3.77
Z_{BU}	16 Ω	$\varepsilon_{r,\perp}$	2.7
$tan\ \delta_{\parallel}$	0.005	$tan\ \delta_{\perp}$	0.012
t	1.3 μm	ε_{reff}	1

The first step is to calculate the main microstrip line parameters and loaded capacitance values, shown in Figure 2.4. By using the primary parameters given in Table 3.1 and the equation 2.3, the per unit length inductance L_t and capacitance C_t are calculated. By using these calculated values and the primary parameters given in Table 3.1, the periodic unit-cell length d, is defined by the equations of 2.2 and 2.6. By using the calculated values of C_r, L_t, C_t, d, and the input Bloch impedance given in Table 3.1, the minimum loaded capacitance and the maximum loaded capacitance will be calculated.

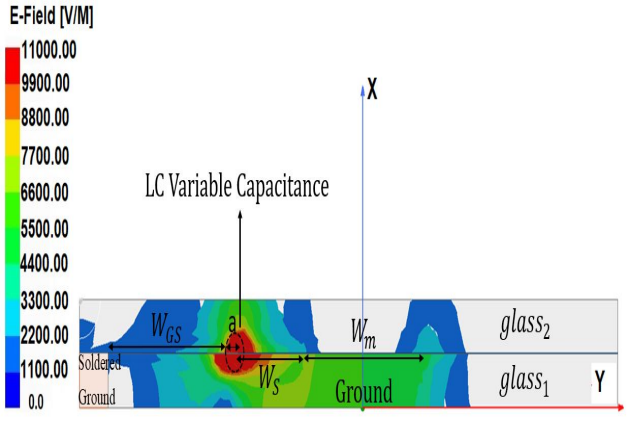

Figure 2.5: HFSS simulated magnitude of E-Field on the cross-side view shown in Figure 2.1c

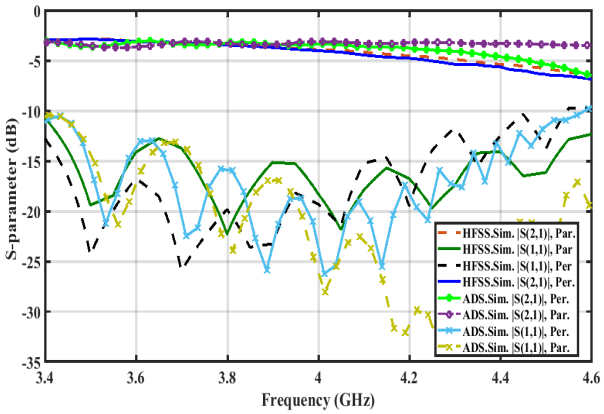

Figure 2.6: S-parameter of the proposed MLCPS versus frequency, calculated with the HFSS full-wave simulation and ADS circuit model simulation, for the perpendicular and parallel case.

The second step, in designing the MLCPS, is finding the value of the stubs and the LC variable capacitance C_{LC} between them, as shown in Figure 2.3. To make our design more convenient with faster optimization in ADS software, an ideal transmission line with $\varepsilon_{eff} = 1$ is assumed in the beginning for all the transmission lines. A 10 unit-cell network, which is created by cascading the two-port circuit model shown in Figure 2.3, is used in ADS optimization. The stubs' values including Z_s, $\theta_S{}^\circ$, Z_{GS}, $\theta_{GS}{}^\circ$, and the LC variable capacitance C_{LC}, are calculated by doing the optimization in ADS. The ADS optimization goal is to make the minimum and the maximum input admittance Y_{in} equal to $j\omega_0 C_{lu}$ and $j\omega_0 C_{lb}$, which have been calculated in the second step. The main microstrip line characteristic impedance Z_0 is given in Table 3.1, and its electrical length θ will be calculated by $\theta = \left(\frac{2\pi}{\lambda_0}\right) * d$, where d is the unit-cell length, derived in the first step. All the parameters in the 10 unit-cell networks, created by cascading the two-port circuit model, are now defined. These known variables are tuned in ADS to achieve the best FOM while the input impedance is matched to Z_{BU}.

In the third step or final step, the ADS optimized values achieved in the second step are converted in HFSS software to find the variables in Figure 2.1. By having the lines' characteristic impedance of Z_0, Z_s, and Z_{GS}, the lines' width and their propagation constant β are defined in the HFSS model. Next, the optimized electrical lengths from the second step including θ° , $\theta_S{}^\circ$, and $\theta_{GS}{}^\circ$, are converted to the lines' dimensions P, W_S, and W_{GS} respectively, based on their related

propagation constant. The LC variable capacitance dimensions a, and b, are defined based on the optimized C_{LC} calculated in the second step.

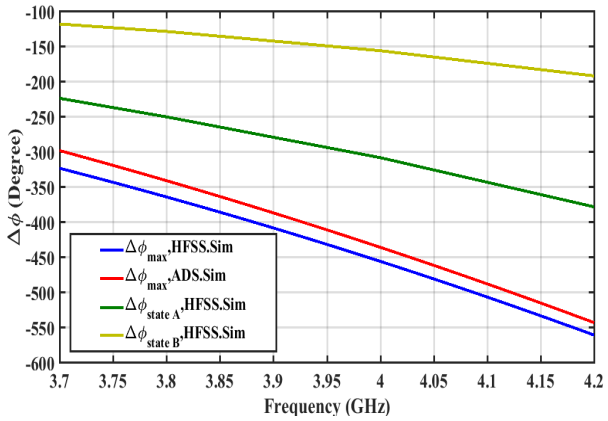

Figure 2.7: The maximum state ($\varepsilon_r = 3.77$), state A ($\varepsilon_r = 3.3$) and state B ($\varepsilon_r = 2.9$) phase-shift relative to the minimum state (ε_r=2.7) , calculated with the HFSS full-wave simulation and ADS circuit model simulation.

Table 2.2: Final Optimized Dimensions of The Proposed MLCPS

W$_m$	2.5 mm	W_S	1.2 mm
P	0.95 mm	l_S	500 μm
l_{GS}	620 μm	L_{tr}	12.2 mm
a	245 μm	b	310 μm
W_{GS}	1.9 mm	W_{tr}	5.55 mm
W_{in}	1.1 mm	L_{in}	5 mm

The two-port network of 10 cascaded unit-cells, shown in Figure 2.1 (b), are optimized in HFSS to have the highest FOM and input matching to Z_{BU} concurrently. To reach a full cycle of phase shift, 360°, 80 unit-cells are implemented in the final MLCPS prototype. A microstrip line transition with dimensions of W_{tr} and L_{tr} is used to match the input impedance of Z_{BU} to 50 Ω. The input impedance of the loaded transmission line without the matching section (Z_{BU}) varies from 16 Ω to 11.7 Ω, while the bias voltage changes from the minimum (2 V_{P-P}) to the maximum value (20 V_{P-P}). The final optimized dimensions of the proposed MLCPS are given

in Table 2.2. The HFSS simulated magnitude of E-Field on the cross-side view of MLCPS is shown in Figure 2.5. The S-parameter of the proposed MLCPS versus frequency, calculated with the HFSS full-wave simulation and ADS circuit model simulation, is shown in Figure 2.6. The maximum phase shift of the proposed MLCPS versus frequency, calculated with the HFSS full-wave simulation and ADS circuit model simulation, is shown in Figure 2.7. The insertion loss lower than 3.95 dB and maximum phase shift of 456.2° are achieved at 4 GHz in the HFSS simulation. The insertion loss lower than 3.35 dB and maximum phase shift of 435° are achieved at 4 GHz in the ADS simulation.

2.2.4 Microstrip Line LCPS Measurement

The prototype of the proposed MLCPS is shown in Figure 2.8. The structures dimensions and specifications are given in Table 3.1 and 2.2. As illustrated in Figure 2.8, the MLCPS is constructed with two layers of glass as a substrate which are attached together in a way that hold the LC material between them. The main microstrip line, loaded periodically with the stubs, is connected to the 50 Ω SMA connector after the microstrip line impedance matching transition. A copper tape, attached to the bottom of glass1 as a main ground, is soldered from the edge (Figure 2.8 (b)) to the $glass_2$, including the periodic metal G-stubs.

The measured S-parameter of the manufactured phase shifter is shown in Figure 2.9. The LC loss varies somewhat linearly from the minimum bias to the maximum bias. The two-port device shows a minimum insertion loss of 3.82 dB and a maximum insertion loss of 4.35 dB for different bias states at center frequency of 4 GHz. The insertion loss at different states are between these two values. In addition, the phase shifter prototype is well matched to 50 Ω from 3.1 GHz to 4.9 GHz, covering the 5G sub-6 band. To measure the phase-shift through the MLCPS, we have used an RF Bias Tee component in series with the phase shifter input to simultaneously apply the RF input and the external bias voltage. A rectangular-shaped pulse with a frequency of 277 Hz is used as an external bias voltage. The measured phase-shift in degrees at 4 GHz versus the applied bias voltage is shown in Figure 2.10. By increasing the peak-to-peak bias voltage from 2 to 20 Volts,

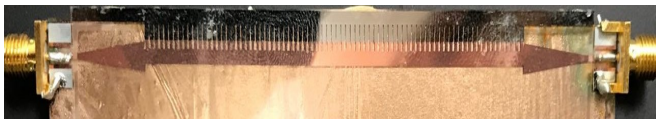

(a) Top-side view

(b) Bottom-side view

Figure 2.8: Manufactured prototype of the proposed MLCPS. (a) Top-side view including a main microstrip transmission line loaded with a variable equivalence capacitance. (b) Bottom-side view including a copper-tape as a main ground, which is soldered from the edge to make a connection with the loaded periodic stubs.

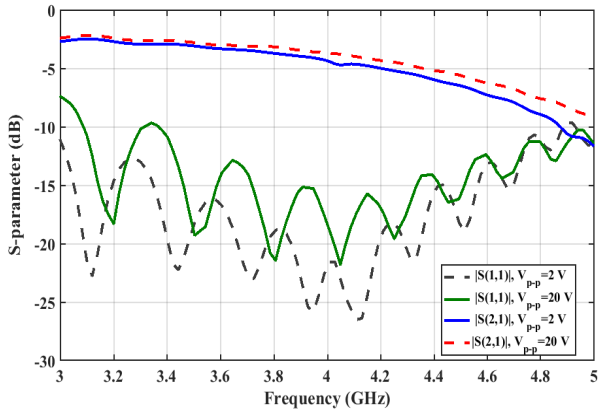

Figure 2.9: Measured S-parameters of the proposed MLCPS.

the amount of phase-shift is increased, and finally a 461° phase-shift is achieved at 20 $Vp-p$. Based on the phase shifter FOM definition given in (2.1), the proposed MLCPS achieved 105.9° $/dB$ at 4 GHz. This MLCPS has 5.76° $/mm$ with the tuning speed of 2 msec. To evaluate the linearity, the two-tone test output power spectrum is measured and shown in Figure 2.11, resulting the OIP3 of 36.1 dBm. There is not any LC-based phase shifter at such a low frequency in the literature which to compare our design, but this result compares with phase shifters designed in the millimeter-wave frequencies, reported in [19]-[20].

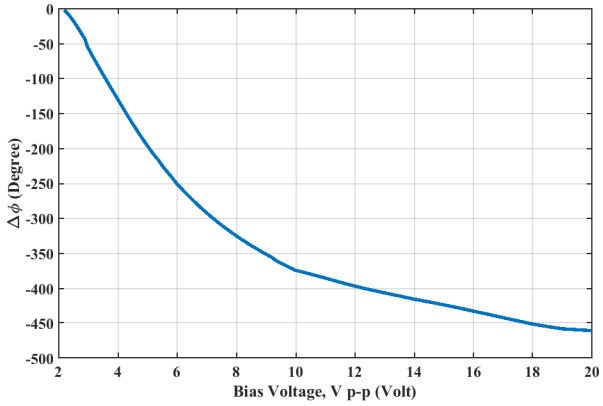

Figure 2.10: Measured phase-shift of the proposed MLCPS versus the peak-to-peak bias voltage at 4 GHz, which is a rectangular-shape pulse with the frequency of 277 Hz.

2.3 LC-based Phased Array Design and Measurement

In this section, an RF phase-shifting phased array system is designed and implemented, as shown in Figure 2.12, to verify the performance of the proposed MLCPS. The phased array system includes an antenna array panel and four-phase-shifter panel, assembled behind the antenna array to make a relative phase-shift in each RF path. The antenna array is constructed with 4×4 aperture-coupled patch antenna elements. By using the equations in [26], the antenna array is designed and optimized in HFSS to cover the sub-6 GHz band, 3.7 GHz to 4.2 GHz . The aperture-coupled patch antenna with optimized dimensions is shown in Figure 2.13a and 2.13b . The radiating patch element is etched on the top of the antenna substrate (AD250c), and the microstrip 50 Ω transmission line is etched on the bottom of the feed substrate (RO4003c). The AD250c has a dielectric constant of 2.52 and loss tangent of 0.0015. The patch length (L_p) and width (W_p) is determined to resonate at the operational center frequency. The coupling level is primarily determined by the length of the coupling slot (L_{slot}), and the tuning stub $(L_{stub})$is used to tune the excess reactance of the slot-coupled antenna, achieving the 50 Ω input matching. As shown in Figure 2.13c, each 4 patch antennas are placed in Y direction with interelement spacing $DY = 45.5$ mm, and are uniformly excited with the microstrip line, which make four antenna sub-arrays. The antenna sub-arrays are placed in Z direction with spacing $DZ = 45mm$, creating a 4-port radiation component. The input

matching and the radiation coupling of the 4-port antenna array are shown in Figure 2.15, resulting in 50 Ω matched ports from 3.2 GHz to 4.4 GHz.

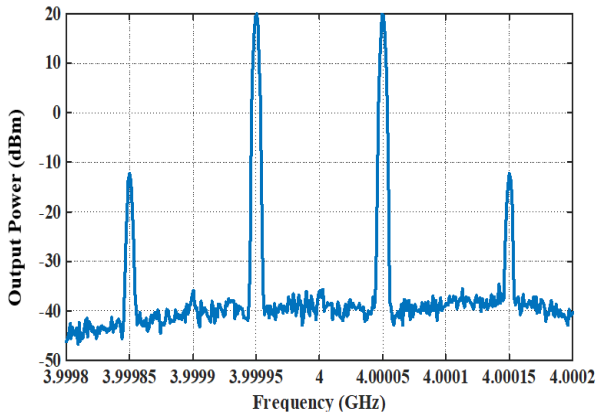

Figure 2.11: Measured two-tone test power spectrum for MLCPS.

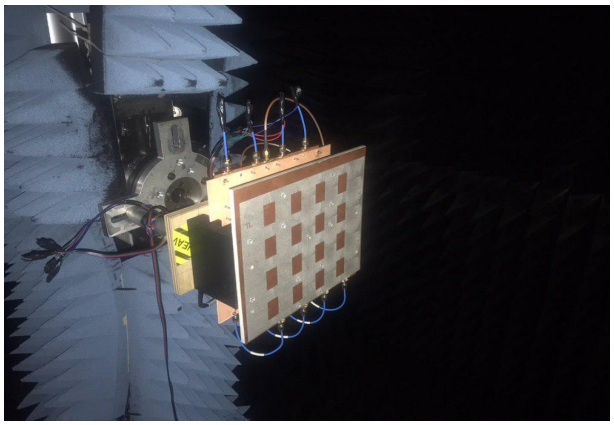

Figure 2.12: RF phase-shifting phased array pattern measurement set-up, by using a 4×4 aperture coupled patch antenna array and a 1×4 proposed phase shifter.

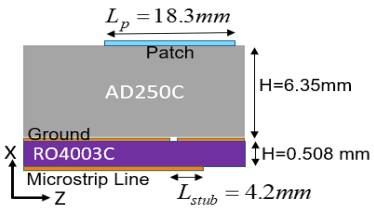

(a)

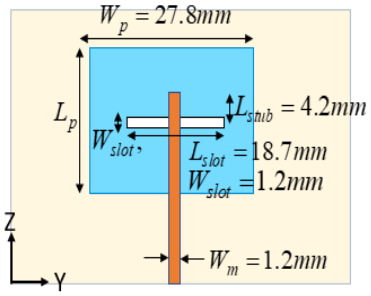

(b)

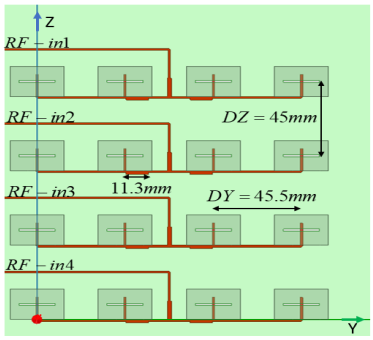

(c)

Figure 2.13: A 4×4 aperture coupled patch antenna array. The patch antenna element designed at 4 GHz, is shown from (a) Side view, and (b) Top view with related dimensions. (c) 4 sub-arrays placed in Z direction, is created by exciting 4 patch antenna elements placed in Y direction.

The phase shifter panel shown in Figure 2.14, includes a 1-to-4 microstrip line power divider to feed the RF field of each phase shifter, mounted on the RO4003 board. This board has a thickness equal to the phase shifter's glass and is cut inside to hold the phase shifter. The ground of the phase shifter is connected to the Rogers board ground layer with copper tape to have a shared ground. The microstrip line on the Rogers board is connected to the phase shifter line by soldering. To combine the RF field and bias voltage, and to control the amount of phase-shift in each phase

shifter, four Mini-Circuits model RCBT-63+ bias tees are integrated at each RF path. The external bias voltages are applied to each Bias Tee from four separate ports, as labeled in Figure 2.14 from Bias1 to Bias4. The RF-INPUT signal is divided into 4 RF-path signals and is added with the bias voltage in the bias tee chips, to excite the phase shifter in each RF path. After being phased shifted in each MLCPS, the four phase-shifted RF signals, Figure 2.14, are connected to the antenna array four input ports with the coaxial cable, Figure 2.13c and Figure 2.12.

The amount of phase-shift needed to have a steered pattern to θ, is given in [27]. To find the bias voltage for each RF pass, the phased array is calibrated by Agilent Network Analyzer (VNA). By applying the external bias voltages in the set-up shown in Figure 2.12, the simulated and the measured normalized radiation patterns are defined and shown in Figure 2.16, and 2.17.

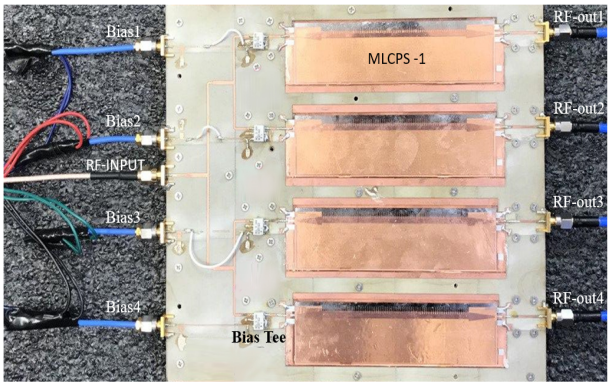

Figure 2.14: The 1×4 array of the proposed MLCPS assembled on the Rogers board with a Bias Tee chip to apply the bias voltage with RF field.

The measured radiation patterns are matched with the simulated patterns in all cases with some discrepancies, especially in sidelobes. This is because of the dissimilarities between the phase shifters' performance created due to the fabrication inaccuracies, which results in a non-uniform feeding network in the antenna array. The antenna array peak gain shows 18.1 dBi at the boresight for the HFSS simulation and 17.3 dBi for the measurement. Nonetheless, the measured result proves the performance of the proposed LC-based phase shifter.

The MLCPS experimental results are compared with the recent phase shifter state-of-art in Table 2.3. As shown in Table 2.3, the proposed phase shifter achieves a high FOM of $105.9^{\circ}\ /dB$ with a full cycle of phase shift. Besides that, the proposed architecture could be integrated on the

PCB board which enables it to be assembled with the antenna platform. In addition, the insertion loss variation with the phase shift is much smaller than the RTPS [5], and the accessible phase resolution is much higher than the STPS [7]. The other parameters of the phase shifter reported in Table 2.3 are either better than or on par with that of previously reported works.

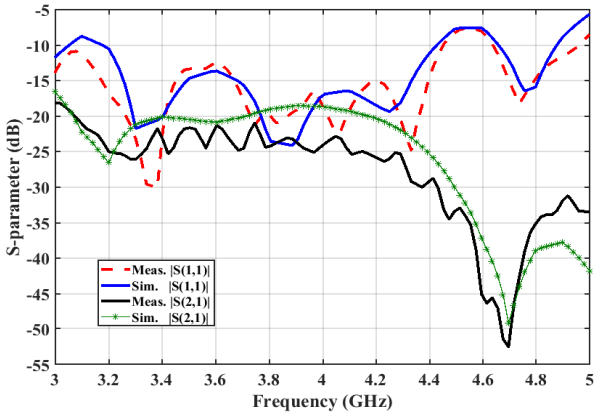

Figure 2.15: Input matching and mutual coupling of the 4-port aperture-coupled patch antenna array, as shown in Figure 2.12-2.13.

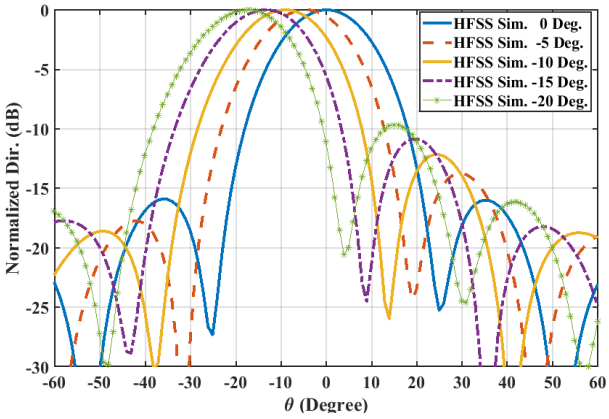

Figure 2.16: Simulated normalized radiation pattern of the phased array at 4 GHz for various beam steering.

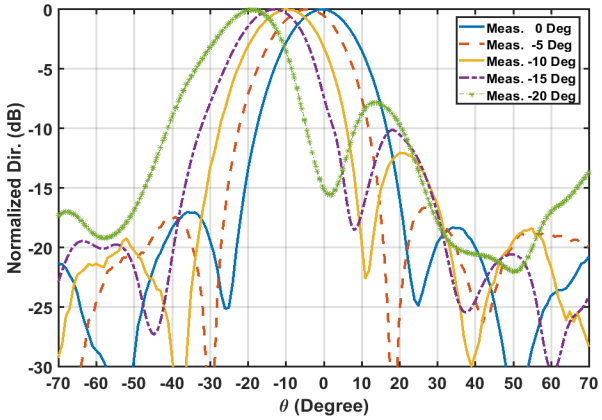

Figure 2.17: Measured normalized radiation pattern of the phased array at 4 GHz.

Table 2.3: Phase Shifter State-Of-The-Art

Technology	Topology	Freq. (GHz)	Delta	Gain	FOM	Power Handling (dBm)	Drive Voltage, Power	Area (mm2)	Ref.
CMOS 65nm	Active, VMPS [1] with Gain Amplifier	25	360	+12.2	\	$\leq$ 10 dBm	12mW	0.052	[4]
CMOS 65nm	Passive, RTPS [2]	29	360	-9.5	37.9	$\leq$ 30 dBm	0 DC power	0.23	[5]
PCB	Passive, RTPS	2	407	-4.4	88	$\geq$ 30 dBm	5 V	4000	[28]
MEMS on PCB	Passive, STPS [3]	2.7	75	-89	84	$\geq$ 30 dBm	N.A	400	[29]
MEMS	Passive, LTPS [4]	30	270	-1.8	150	$\geq$ 30 dBm	16 V	30	[6]
CMOS 65 nm	Passive, STPS	28	360	-6.36	56.6	$\leq$ 10 dBm	1 V	0.23	[7]
Ferroelectric (BLT [5])	Passive, GCPW line under BLT slab	20	210	-1.4	221.4	$\gg$ 30 dBm	22mW	60	[8]
Ferrite on PCB	Passive, Microstrip line under Ferrite	3.3	679.9	-30	22.6	$\gg$ 30dBm	100 KA/m	3551	[30]
Liquid Crystal	Passive, Microstrip delay line	17.5	N.A	-4	62.5	$\geq$ 30 dBm	25 V	350	[19]
Liquid Crystal	Passive, CPW LTPS	20	90	-1.5	60	$\geq$ 30 dBm	40 V	NA	[20]
Liquid Crystal	Passive, Microstrip LTPS	17	30	-1	30	$\geq$ 30 dBm	20 V	NA	[31]
Liquid Crystal	Passive, Loaded Dielectric Waveguide	75	360	-3.6	100	$\geq$ 30 dBm	250 V	112.5	[32]
Liquid Crystal	Passive, Microstrip RTPS	35	270	-7	38.5	$\geq$ 30 dBm	25 V	NA	[33]
Liquid Crystal	Passive, Microstrip LTPS	28.4	400	-7.4	54	$\geq$ 30 dBm	5 V	NA	[34]
Liquid Crystal	Passive, A novel LTPS architecture	4	461	-4.31	105.9	$\geq$ 30 dBm	0 DC power, 20 Vp-p	616	This Work

[1]Vector Modulator Phase Shifter, [2]Reflection-Type Phase Shifter,

[3]Switched Transmission Line Phase Shifter, [4]Loaded Transmission Line Phase Shifter,

[5]Barium Strontium Titanate

Chapter 3

TVTL MIXER-FIRST PHASED ARRAY RECEIVER FOR SPACE FREQUENCY INTERFERENCE REJECTION

3.1 Introduction

For several decades, phased arrays have been primarily utilized in military applications; however, ongoing research is focused on proposing a low-cost, low-power, low noise and highly linear phased array system for commercial use. Furthermore, advanced phased array or beamforming systems have been developed to achieve higher effective isotropic radiated power (EIRP) in transmitters and lower noise figures (NF) in receivers, thereby enabling higher data rates and system capacity in wireless communications [35]. The phased array receiver has three different phase-shifting architecture implementations categorized based on the location of the phase shifter stage in the system: RF-path, LO-path, and IF-path [36]. Trade-offs between the three implementations are discussed in [37]. The LO-path phase-shifting architecture is considered advantageous since the loss, non-linearity, noise performance, and bandwidth of the phase shifters do not directly impact the system performance, as they are not placed in the signal path. Additionally, the excitation amplitude of each antenna element does not significantly vary with various phase-shift settings since the LO-path works in saturation.

The growth of wireless traffic, due to an increase in channel bandwidth, the number of bands, and the use of parallel receivers/transmitters in wireless communication, has resulted in both in-band and out-of-band interference, which can significantly degrade receiver linearity and noise performance. Strong blockers in the receiving band can also affect the linearity of the LNA in the conventional receiver. To address these issues, a first stage of surface acoustic wave (SAW) filters

is often used in the conventional RF-Front-End architecture to eliminate strong out-of-band blockers. While these filters result in good linearity, they cannot isolate in-band interference/jammer, and their frequency is not programmable. Another approach proposed in [38]-[41] is switched capacitor based frequency translational technique (N-path filter), which can realize tunable filters at the price of spurious emission and low power handling.

Recently, the mixer-first receiver architecture has attracted the attention of researchers [42]-[43]. In [44], a passive current-mode mixer-first receiver is proposed, which employs a regulated cascode-based filtering trans-impedance amplifier immediately after the mixer. This approach improves linearity for out-of-band interference and achieves a P1dB of $+3\ dBm$, a noise figure of $5.5\ dB$, and a power consumption of $21.6\ mW$. Conversely, the active mixer [42] offers a higher conversion gain of $12.1dB$ with a high noise figure of $6.5\ dB$ over its bandwidth, but it has a low $P1dB$ compression point of $-5\ dBm$. Therefore, both passive and active mixers have poor noise performance and linearity, which can degrade the performance of the mixer-first receiver front-end. The parametric-amplification mixer [45]-[46] uses nonlinear or time-varying reactance for signal amplification or frequency conversion, providing a low-noise amplification approach. Mixer-first receivers have recently gained attention, and devices based on parametric mixing, such as the time-varying transmission line (TVTL), have been proposed for their low noise characteristics and broadband behavior [47, 48]. Compared to typical low noise amplifiers, a TVTL chip typically has a much higher P1dB of over $10\ dBm$, making a TVTL mixer-first receiver more robust to co-site interferences or blockers from nearby transmitters.

This chapter introduces a new mixer-first phased array receiver that utilizes a modified linear TVTL mixer [49] to suppress both in-band interference with a different direction of arrival (DoA) and out-of-band interference in general. The architecture proposed in this study, shown in Figure 3.1, uses the highly linear TVTL mixer with a $P1dB$ of $12\ dBm$ as the first stage, resulting in a more robust phased array receiver than the LNA-first conventional receiver. The in-band interference ($Blocker2$) originating from a different direction than the received signal is effectively canceled after the mixer by employing the LO-phase shifting mechanism. Meanwhile, a fixed

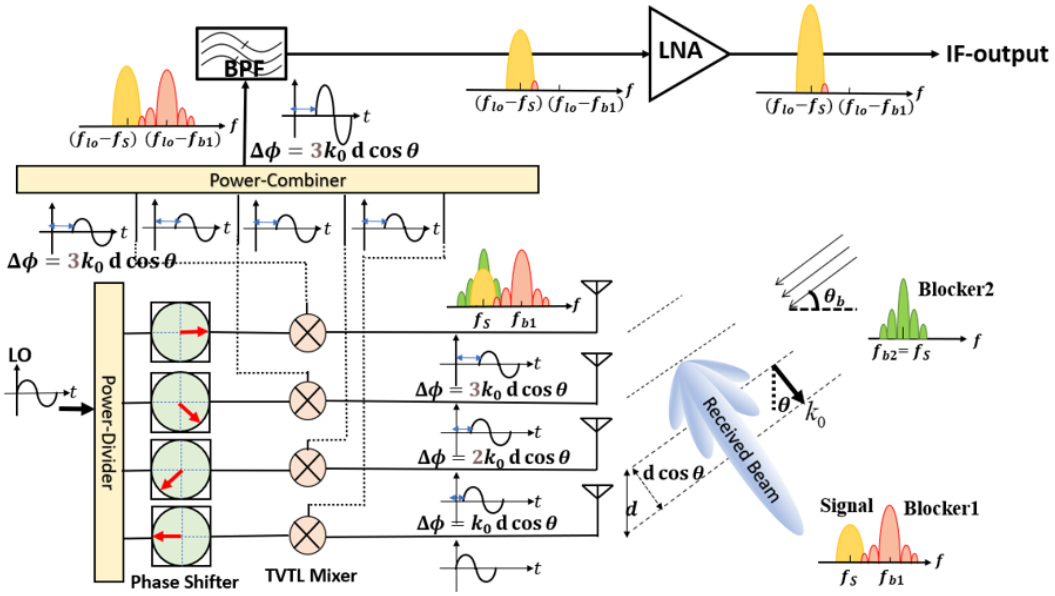

Figure 3.1: Mixer-first phased array receiver architecture.

pass-band filter is used to reject out-of-band interference that shares the same direction of arrival as the received signal ($Blocker1$), while the LO is tuned to maintain the input interference frequency within the filter rejection band. Therefore, the proposed architecture allows the receiver to tolerate and eliminate in-band and out-of-band spatial interference before saturating the LNA. Additionally, since the input RF signal is not affected by the phase shifter, the proposed LO phase shifting architecture provides better noise figure performance.

3.2 Phased Array Receiver: Design And Implementation

3.2.1 Phased Array Receiver Architecture

The proposed architecture of the phased array receiver is depicted in Figure 3.1, and its performance is validated through the implemented demo, as illustrated in Figure 4.6. The main signal beam, centered at f_s and arriving from direction θ, is clearly defined. In-band interference, denoted as Blocker2, is also centered at f_s but arriving from a different direction θ_b. On the other hand, out-of-band interference, called Blocker1, arrives from the same direction as the main signal θ. The antenna array receives the main signal, in-band and out-of-band interference, as shown in the

spectrum of Figure 3.1. To steer and shape the radiation pattern electronically, each antenna element is excited with a relative phase-shift. This relative phase-shift is applied to the received signal at each antenna element to make them coherent, resulting in a maximum signal-to-noise ratio. The relative phase-shift ($k_0 d\cos\theta$) is a function of the incoming main signal direction of arrival θ, the distance between antenna elements d, and the wave number at the center frequency of f_s.

The performance of phased arrays can be classified based on where the relative phase-shift is applied, such as RF-path, LO-path, and IF-path types. However, each type has its own trade-offs. In the proposed architecture shown in Figures 3.1 and 4.6, the phase-shift stage is applied in the LO-path to ensure that the performance of the phase shifter does not affect the receiver's noise figure and linearity. A lossy liquid crystal phase shifter (LCPS) [50] is used as a phase shifter in this chapter. The LO signal is divided using a power divider and reaches the phase shifters coherently with the same phase and amplitude. The LCPS creates a relative phase-shift in response to the input bias voltage. The RF phase-shifted signals from the antenna elements are multiplied by the LO phase-shifted signals in the TVTL mixer, generating coherent converted signals that are combined in a power combiner to produce an output IF signal.

In conventional RF front-ends, the Low-Noise Amplifier (LNA) is usually utilized as the first stage to amplify signals and enhance signal detection. However, the low linearity of the LNA-first receiver renders it incapable of handling strong Blocker1 and Blocker2 signals picked up by the antenna element. In contrast, the proposed architecture positions a parametric mixer (TVTL) [49] with a high input referred P1dB of $12\ dBm$ and a noise figure of $3\ dB$ as the first stage following the antenna. The proposed mixer has a substantially higher P1dB ($12\ dBm$) than a typical LNA, thereby enabling the first-mixer phased array receiver to tolerate and eliminate strong in-band and out-of-band spatial interference/jammer without affecting the noise figure. By converting the input RF signal frequency to the pass-band of a fixed filter, the mixer makes them coherent by applying the relative phase shift.

In-band interference (Blocker2) is canceled after the mixer by using the LO-phase shifting mechanism. Out-of-band interference (Blocker1) is rejected by using the fixed pass-band filter,

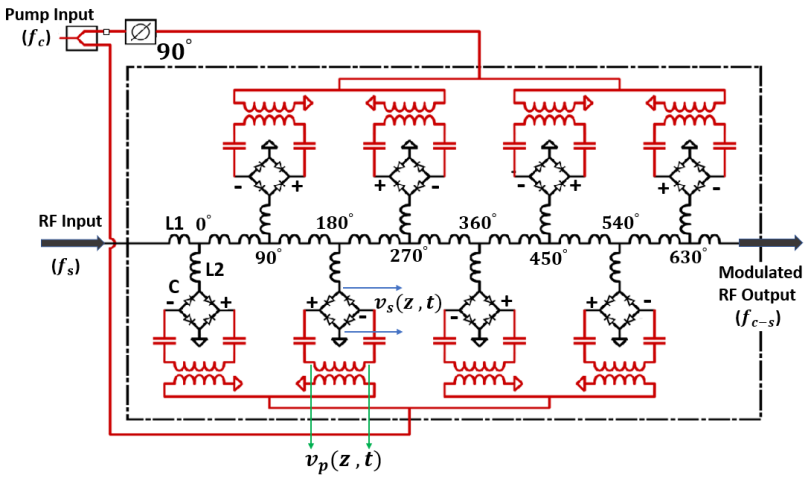

Figure 3.2: Circuit model of traveling wave direct-pumped TVTL featuring phase match at the varactor diode bridges, driven by the signal and pump independently from the balanced ports.

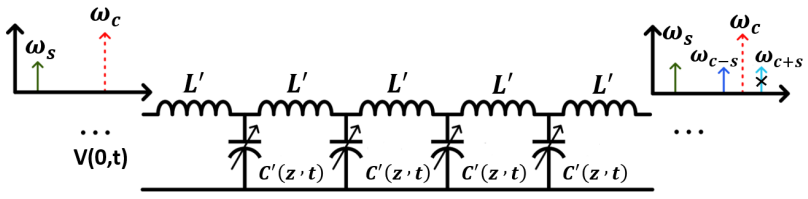

Figure 3.3: Simplified Lumped-element model of the Figure 3.2 with time-varying capacitance.

while the input frequency is tuned by the LO to always see the filter rejection band. After the spatial interference rejection, only the main signal reaches the LNA. This means that the proposed architecture is considered advantageous in terms of linearity. Furthermore, by using the low noise TVTL mixer with gain as the first stage between the RF-INPUT and the IF-OUTPUT, we can achieve low noise figure and highly linear receiver. On the other hand, the receiver noise figure is not deteriorated by the loss of the phase shifter placed in LO-path. The liquid crystal phase shifters are low-power and low-cost component, which does not consume the DC power. These properties allow to achieve a linear and low power hardware to implement the phased array receiver for wireless commercial application.

3.2.2 MMIC TVTL Mixer

The proposed receiver architecture utilizes a MMIC TVTL mixer as its first stage, which can be seen in Figure 3.7 [49]. The TVTL circuit schematic is illustrated in Figure 3.2. This single-

sided directly-pump TVTL mixer comprises a traveling transmission line loaded with a varactor bridge that functions as a voltage-dependent time-varying capacitance ($C'(z,t)$). It should be noted that the pump voltage ($v_p(z,t)$), rather than the pump power, is responsible for the time-varying capacitance of the varactor bridge, necessitating a signal and pump path that is isolated from one another. The balanced nature of the bridge provides isolation, with the pump power modulating the capacitance of the varactor diode without being coupled to the transmission line. The pump is divided into two parallel splitting networks and supplies the diode bridges differentially from both the top and bottom sides. The signal ($v_s(z,t)$) travels along the transmission line, which is insulated from the pump voltage, and the pump power only experiences a lossless capacitive load when the resistive loss of the varactor diode and the energy converted to other frequencies are negligible. To achieve the phase matching condition at only the varactor diode bridges, the pump is initially divided by a 90-degree hybrid to create the necessary 90-degree phase shifts, and the connections of the balun that feeds into the diode bridge in the pump path are reversed to obtain the 180-degree phase shifts.

To comprehend the proposed TVTL's theory and performance, the circuit schematic in Figure 3.2 is simplified using lumped elements, as shown in Figure 3.3. The traveling wave TVTL's theory is explained in [49], [51]. A linear and time-variant differential equation for signal voltage along the traveling transmission line is derived by assuming $|v_s| \ll |v_p|$ and non-distributed propagation of the pump signal on the transmission line. This equation is given by:

$$\frac{\partial^2 \, v_s \, (z,t)}{\partial z^2} = L' \frac{\partial}{\partial t} \left\{ \frac{\partial C'(z,t) v_s(z,t)}{\partial t} \right\} \tag{3.1}$$

where the voltage dependant time-varing capacitance ($C'(z,t)$), and the pump voltage signal is defined by :

$$C^{'}(z,t) = C_0 + C_1 V_p cos(\omega_p t - \beta_p z + \phi_p) \tag{3.2}$$

$$v_p(z,t) = V_p cos(\omega_p t - \beta_p z + \phi_p) \tag{3.3}$$

The solution of the time-variant equation (3.1) only exists [52], when the phase matching condition in a discrete form holds with a constant phase velocity $V_p v$, i.e:

$$V_{pv} = \frac{\omega_s}{\beta_s \Delta z} = \frac{\omega_{c-s}}{\beta_{c-s}\Delta z} = \frac{\omega_c}{\beta_c \Delta z} = \frac{\omega_p}{90^o} \tag{3.4}$$

For the TVTL chip shown in Figure 3.7, the the delay of each splitting pump path is created by the linear progressive phase shift of 90-degree phase interval, as shown in Figure 3.2. The phase delay of the signal through each unit with length of (Δz) can be designed to observe the phase matching condition ($\frac{\omega_s}{\beta_s \Delta z} = \frac{\omega_p}{90^\circ}$).

The voltage gain of the upconverted signal under single sideband mixing condition can be obtain [51] as :

$$G_c = \sqrt{\frac{\beta_{p-s}}{\beta_s}} \sinh\left(\frac{1}{4}\xi\sqrt{\beta_s \beta_{p-s}} z\right) \tag{3.5}$$

where ξ is the modulation index defined as $\xi = V_p C_1/C_0$, z represents the length of the transmission line, and $\beta_s, \beta_{(p\pm s)}$ represent the phase constant of the signal wave and upconverted signal wave. A larger capacitance modulation index ξ or a larger $\beta_{c\pm s}/\beta s$ can lead to a larger conversion gain. This indicates that the conversion gain would increase with an increase in the pump voltage or the frequency separation between $\omega(p \pm s)$ and ω_s.

3.2.3 Liquid Crystal Phase Shifter

The proposed first-mixer phased array receiver utilizes the microstrip line liquid crystal phase shifter (MLCPS) as a phase-shift stage, as depicted in Figure 3.1 and 4.6, which was introduced in [50]. This phase shifter is based on a main microstrip line, periodically loaded with an equivalent capacitance observed from shunt microstrip stubs. The dielectric material used for this loaded

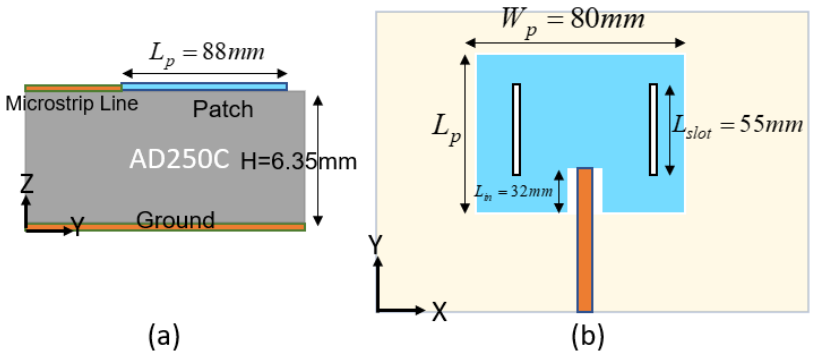

Figure 3.4: The patch antenna element geometry with optimized parameters. (a) Top-view (b) Side-view.

capacitance is a Nematic Liquid Crystal [53], whose permittivity changes with the applied bias voltage. This tunable dielectric creates a variable capacitance that can be loaded periodically onto the microstrip line and can cause a phase shift by altering the transmission line phase constant. The MLCPS design and measurement have been discussed in detail in [50]. The phase-shift stage includes a 1-to-4 power divider, four MLCPSs, and four Bias Tee components from the RCBT-63+ model. To achieve a desired relative phase-shift in each of the four LO-paths, a separate bias voltage is applied to each MLCPS, as labeled in Figure 4.6 from Bias-1 to Bias-4.

3.2.4 Patch Antenna Array

To evaluate the performance of the proposed phased array architecture, a four-element patch antenna array is designed and optimized using HFSS software. The optimized patch antenna element dimensions are shown in Figure 3.4. The S-parameters of the patch antenna element are measured and simulated, as shown in Figure 3.5, and indicate a good match to 50 Ohm at 1 GHz. The two slots etched in patch antenna helps the antenna input matching. The antenna array consists of four of these patch antenna elements with an inter-element spacing of d=150mm, as shown in Figure 4.6.

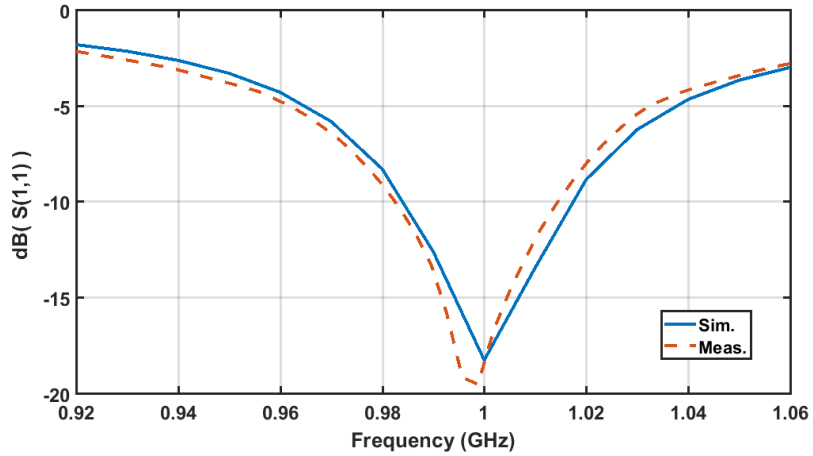

Figure 3.5: Input matching of the patch antenna element

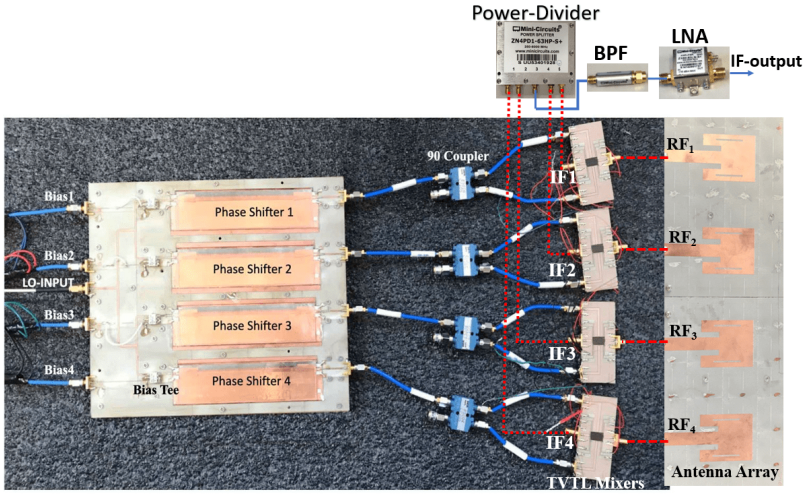

Figure 3.6: First-mixer phased array receiver implementation.

3.3 Measurement Results

This section describes the design and implementation of the LO-phase-shifting phased array to validate the performance of the proposed mixer-first phased array receiver, as depicted in Figure 3.1 and 4.6. The implementation of the four-element phased array receiver involves the use of four mixer chips based on TVTL technology [49], four liquid crystal phase shifters [50] as the phase-shift stage, and a four-element patch antenna array as the radiating component, as depicted in Figure 3.1 and 4.6.

The Advanced Wireless Semiconductor Company (AWSC) 1um GaAs HBT process was used

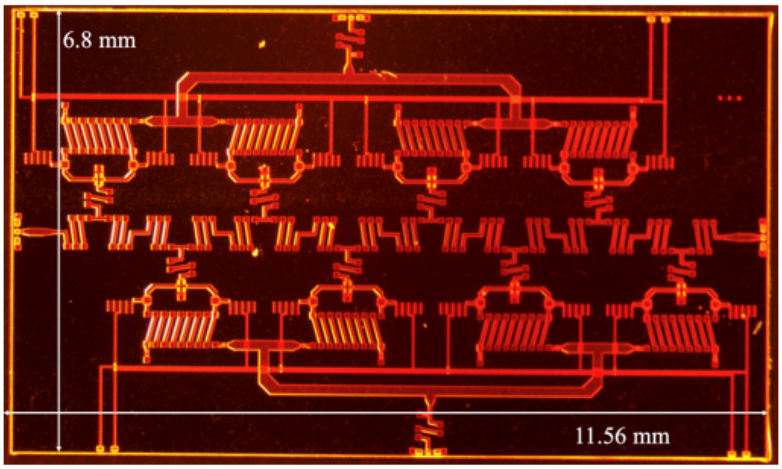

(a)

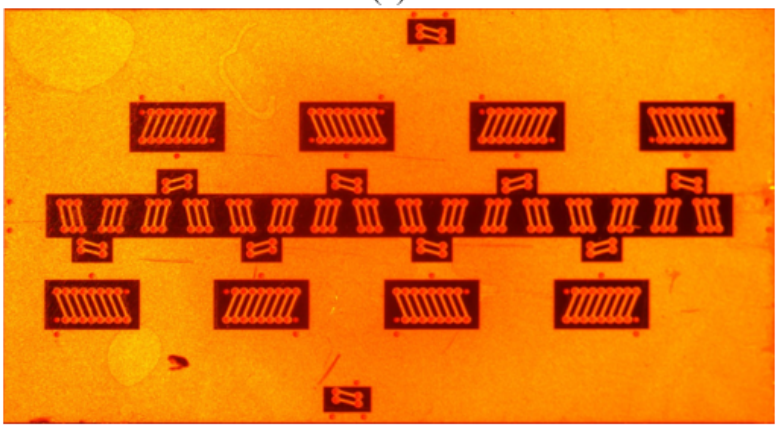

(b)

Figure 3.7: Picture of the fabricated direct-pumped TVTL MMIC (a) Top view (b) Bottom view.

to design and fabricate this directly-pumped TVTL with planar solenoid inductors. The photo of the designed TVTL MMIC is shown in Figure 3.7, and the chip size measures $11.56mm \times 6.8mm$. The TVTL mixer port-to-port isolation is shown in Figure 3.8. Within the RF input signal frequency lower than 2 GHz, the mixer exhibits 20 dB of RF-IF isolation. When operating at a LO signal frequency of 4 GHz, the mixer achieves 30 dB of LO-RF and LO-IF isolation. The results of the measurements for the DP-TVTL, along with theoretical and simulation data, are presented in Figure 3.9, which shows the double sideband (DSB) noise figure. Figure 3.10 displays the conversion gain of the MMIC versus the input power, which was measured to test its power handling performance. The measured spectrum at the output of the direct-pumped TVTL under the 2-tone test is shown in Figure 3.11, which is used to calculate the IIP3. As a parametric

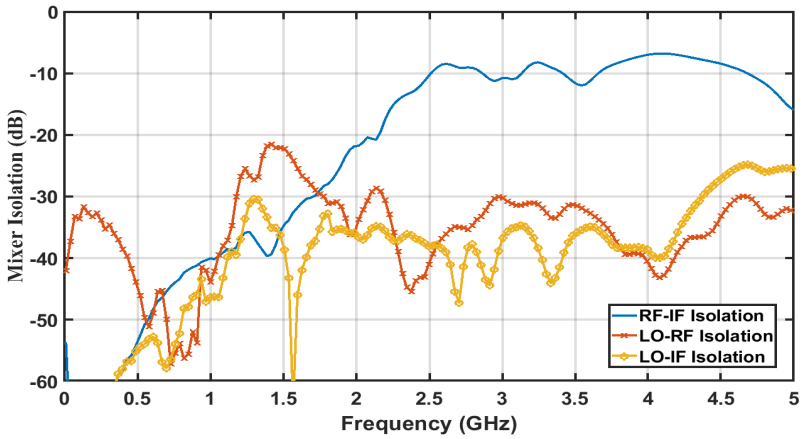

Figure 3.8: Measured port-to-port isolation (S-parameter) of the designed direct-pumped TVTL with varactor biased at -5.0V.

mixer, the MMIC TVTL achieved a low noise figure of 3dB, an input referred P1dB of 12 dBm, and an input referred third-order intercept point (IIP3) of 22.5 dBm. The P1dB can be increased to approximately 18 dBm by optimizing the impedance matching, as shown in the third curve in Figure 3.10. Additionally, the measured insertion loss (S21) and return loss (S11) of the TVTL with varactor diodes biased at -5.0V indicate good matching and insertion loss up to the TVTL's cutoff frequency (3 GHz). The LO frequency or pump frequency used in this experiment is set at 3.2 GHz, while the RF signal is received by the patch antenna array at 1 GHz.

The performance of the proposed directly-pumped TVTL is compared to other recently published mixers in TABLE 3.1. The Analog Device HMC334LP4E passive mixer designed based on SiGe technology achieves a higher IIP3 of 26 dBm, but at the cost of high conversion loss (-1dB) and poor noise figure (8dB). The active mixers proposed based on CMOS technology [54]-[55] offer higher positive conversion gain, but with low IIP3 and poor noise figure. Therefore, the overall comparison shows that the TVTL mixer in [49] has the best performance for the mixer-first phased array receiver, as it has a high IIP3 and low noise figure.

The required bias voltages for a 1-D electronically steered phased-array antenna are provided in TABLE 3.2. The amount of phase-shift required to steer the pattern to a desired angle, as stated in [58], is also given. However, due to fabrication defects during the manufacturing process of the MLCPS, the performance of the phase shifters is not identical, and the input RF signal and

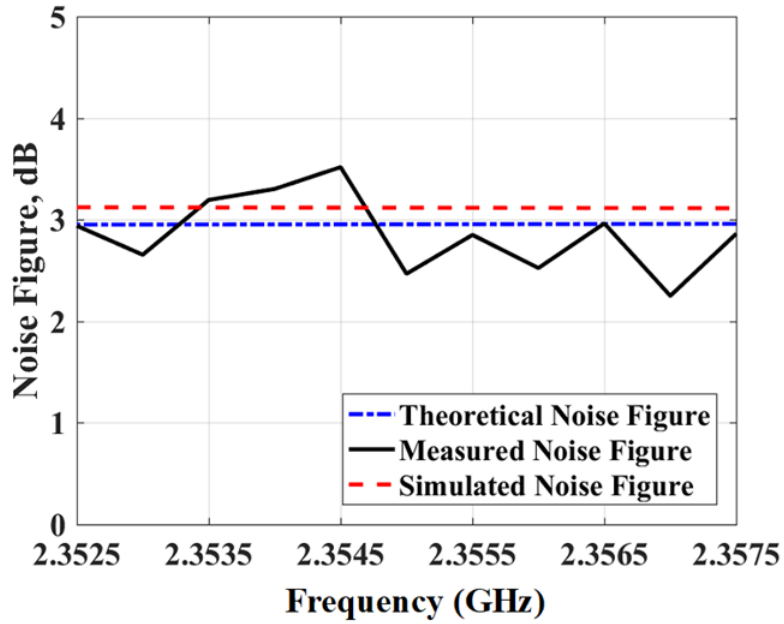

Figure 3.9: Measured DSB noise figure of the DP-TVTL in comparison with the theoretical and simulation results.

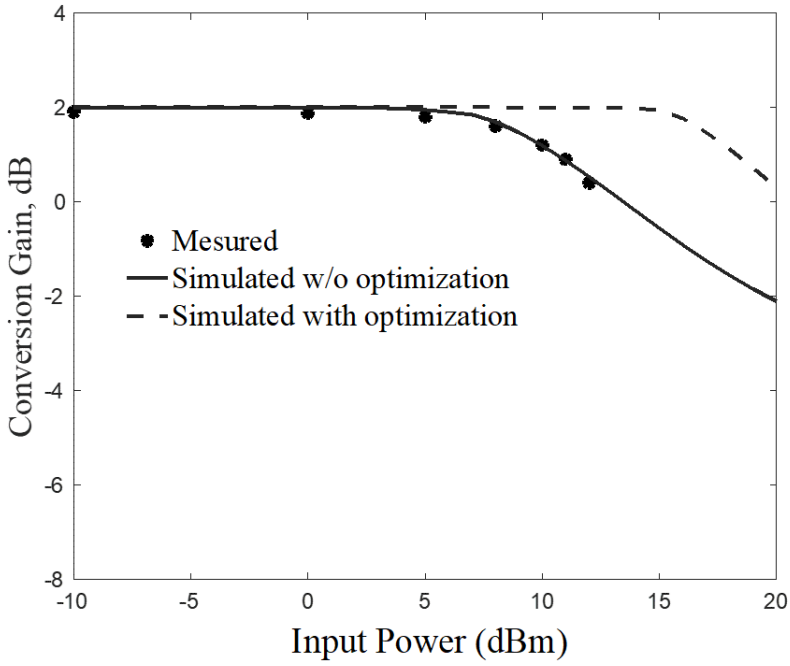

Figure 3.10: Measured conversion gain of the DP-TVTL versus the input power versus the simulated and optimized results.

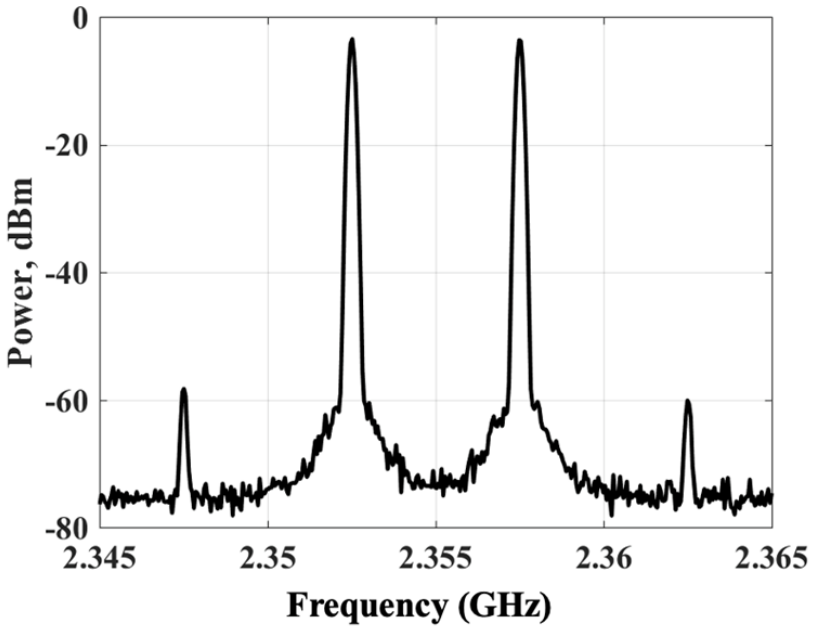

Figure 3.11: Measured spectrum at the output of the direct-pumped TVTL under the 2-tone test, with varactor diodes biased at -5.0V.

Table 3.1: Mixer State-Of-The-Art

Mixer	MDA4 -752H+ [1]	334LP4E [2]	[56]	[57]	[54]	[55]	[46]	[49] This Work
Technology	InGap HBT	SiGe	PCB GaAs Diodes[3]	0.2um GaN HEMT[3]	CMOS 65nm	CMOS 0.13um	PCB GaAs Diodes[3]	1um GaAs HBT[3]
RF Center Frequency (GHz)	3.85	1.65	1.1	6	3.5	3.1	1.9	0.9
Conversion Gain (dB)	7.6	-1	-2	1.8	18	15	10	3
NF (dB)	8.6	8	1	6	5	4.2	3.3	3
IIP3 (dBm)	16	26	20	N/A	-3	2.5	16	22.5
DC Power (mW)	705	865	0	0	16	25.5	0	0
Pump Power (dBm)	0	0	26	21.5	14.5	-2	27	31

[1]Mini-Circuits, MDA4-752H+, [2]Analog Device, HMC334LP4E,
[3]Designed Based on Parametric Amplification Theory,

output IF signal have different frequencies. Therefore, a modified method is used for phase calibration. A Digital Serial Analyzer Sampling Oscilloscope is employed to measure the relative phase-difference between the LO-paths. The 1-to-4 power combiner used in the IF-path is removed and replaced by the patch antenna array in the RF-path. The input of the power divider is connected to an RF Signal Generator, and the four output ports are connected to the respective TVTL RF port. The four IF output ports are connected to the Oscilloscope ports sequentially. The Oscilloscope port connected to the first LO phase-shifting pass controlled by Bias1 is set as the reference port in the Oscilloscope set-up, which is designed to display the phase difference

Table 3.2: Measured bias voltages from phase calibration to have steered pattern at (a) $\theta = -10^{\circ}$, and (b) $\theta = -20^{\circ}$.

(a)

Phase-Shift (deg.)	Bias Number	Vp-p (V)
0	1(Blue)	2.90
-35	2(Red)	2.82
-70	3(Green)	4.31
-105	4(Black)	2.98

(b)

Phase-Shift (deg.)	Bias Number	Vp-p (V)
0	1(Blue)	2.90
-69	2(Red)	3.03
-137	3(Green)	5.18
-206(154)	4(Black)	3.67

between the reference port and the other ports. The bias voltages, labeled from Bias1 to Bias4, are then adjusted to achieve the relative phase difference shown in Figure 3.12 on the oscilloscope screen. The calibrated bias voltages are listed in TABLE 3.2. The Oscilloscope screen set-up for the phase calibration is displayed in Figure 3.12, and a steered pattern at $\theta = 20^{\circ}$ is achieved. The peak antenna array gain is equal to 11.8 dBi at boresight.

The bias voltages are not increased in a sequential order, which is due to the MLCPS manufacturing defects. Using the bias voltage values presented in Table 3.2 and the set-up illustrated in Figure 4.6, the far-field radiation patterns are measured and depicted in Figure 3.13 for various phase-shift mechanisms. The phased array measurement demonstrates a continuous beam scanning over the elevation angle of 0° to 20°. This outcome confirms the efficacy of the proposed mixer-first phased array receiver architecture.

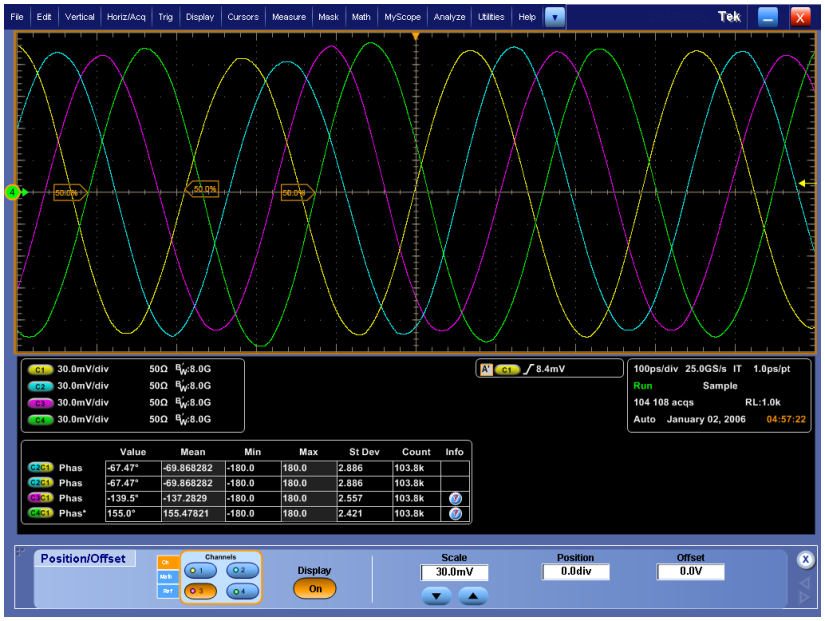

Figure 3.12: The Oscilloscope screen set-up for the phase calibration to have a steered pattern at $\theta = -20°$.

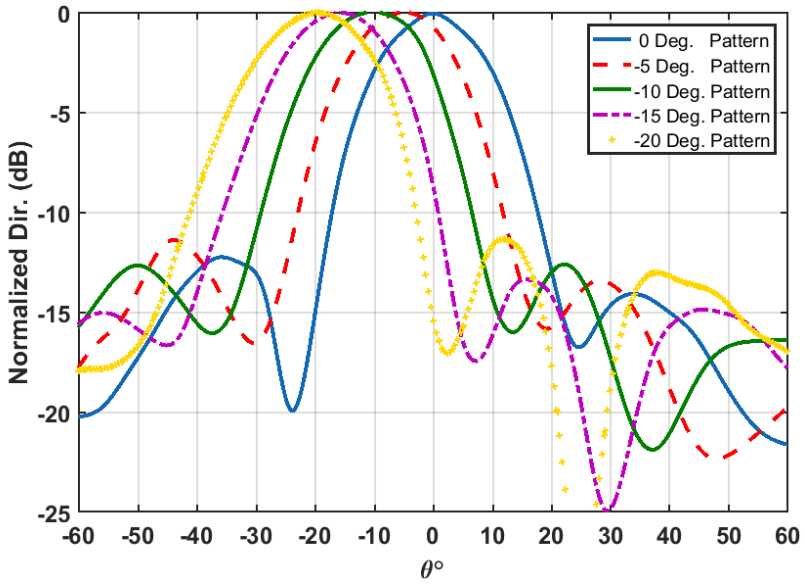

Figure 3.13: Measured normalized radiation pattern of the proposed mixer-first phased array. The calibrated LC-phase shifter bias voltages for $\theta = -10°$ and $\theta = -20°$ pattern are given in TABLE II.

Chapter 4

DUAL-BEAM 2D-SCANNING PHASED ARRAY ARCHITECTURE FOR SATELLITE COMMUNICATIONS

4.1 Introduction

Satellite communication (SATCOM) is crucial for the evolving landscape of 5G and 6G telecommunications, providing high-speed, reliable connectivity in areas with limited terrestrial access. SATCOM is poised to address communication needs in remote regions, supporting IoT applications like autonomous vehicles, smart cities, and disaster response. As demand for high-bandwidth communication grows, integrating SATCOM with next-gen networks will enhance global coverage and efficiency, benefiting various industries [59]-[60].

In Low-Earth Orbit (LEO) SATCOM, a flexible ground station receiver with wide scanning capabilities is essential. A multi-beam phased array receiver, such as the one proposed in [61]-[62], employs beamforming to track and communicate with multiple satellites simultaneously. This approach minimizes signal interference, increases bandwidth, and meets urgent communication needs.

Various phased array architectures exist, including analog, hybrid, and fully digital beamforming (DBF). Each has specific advantages and disadvantages, with DBF offering superior flexibility but facing challenges like high power consumption and cost due to its need for a distinct radio frequency chain per antenna. Hybrid beamforming (HBF) combines analog and digital elements, reducing costs and power consumption compared to full DBF [63].

Analog beamforming, categorized as active phase shifter-based and passive network-based, presents advantages of wide bandwidth and low power consumption. Active phase shifter-based

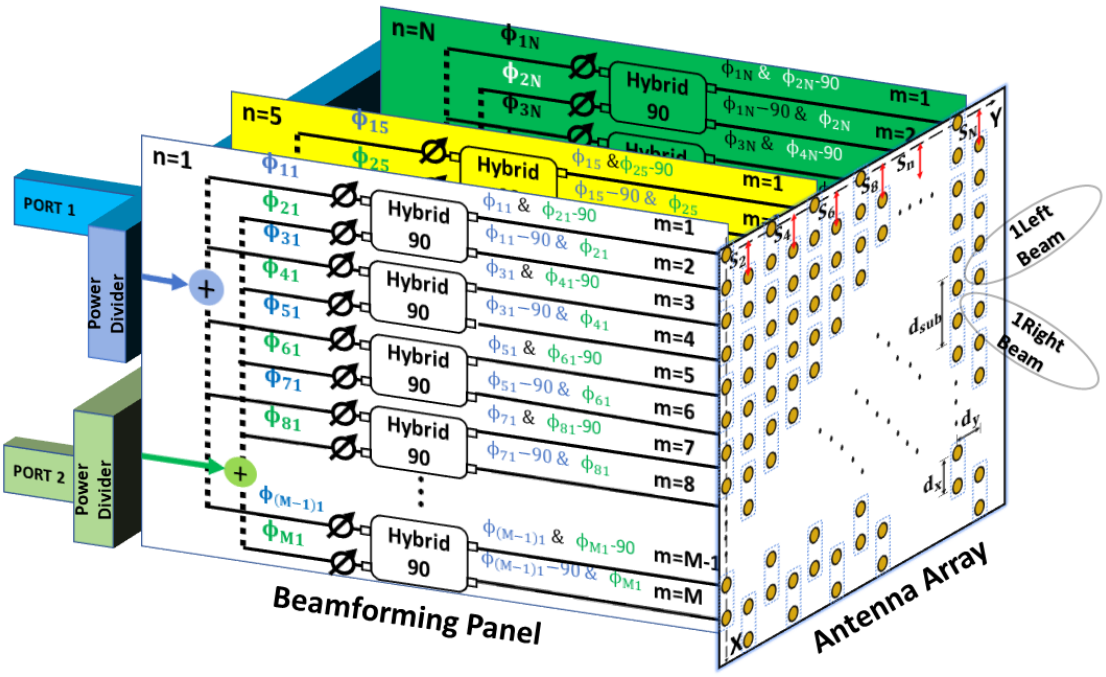

Figure 4.1: Dual-beam 2D-scanning phased array architecture.

beamforming adjusts beam signals using analog components, widely used in SATCOM due to the low cost of integrating beamforming networks (BFN) in CMOS technology. However, its cost and complexity increase with multiple simultaneous beams.

Passive network-based beamforming involves circuits integrated into a single substrate, utilizing structures like Butler matrices or Rotman lenses. Butler matrices are passive and power-efficient, creating fixed beams, while Rotman lenses provide phase shifts for beam switching. However, these networks face challenges with increasing antenna elements, leading to complexity and feeding network losses.

To overcome these challenges, a new multi-beam phased array (MBPA) architecture is proposed in this chapter. The scalable, low-complexity architecture achieves dual-beam 2D-scanning phased arrays, utilizing 90-degree hybrid blocks for sub-arrays. Linear-progressive phase shifters control in-phase and quadrature-phase signals, enabling concurrent independent beams without dividing the aperture. To address grating lobes along the X-axis, the chapter suggests shifting

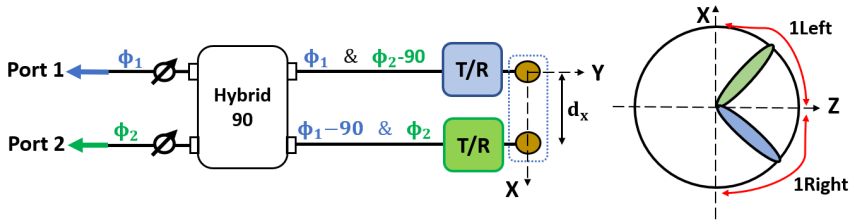

Figure 4.2: The principle of generating orthogonal beams using 90-hybrid coupler.

antenna array columns, optimizing shifts to reduce grating lobes and maintain maximum antenna matching bandwidth. Simulation and measurement results demonstrate the proposed architecture's scalability to large arrays without compromising performance.

4.2 Phased Array Architecture Theory and Design

The proposed MBPA architecture, illustrated in Figure 4.1, utilizes an $N \times M$ planar antenna array for high gain, directive radiation, and precise signal control. It consists of a beam-forming panel, power dividers, and antenna elements. The 90-degree hybrids in the beamforming panel generate I/Q signals for dual-beam transmission, and the phase shifter enables versatile 2D-scanning. The power divider enhances signal strength by summing independent beams. The MBPA excels in creating multiple beams, offering superior coverage and signal quality. Its fast scanning capabilities make it ideal for high-speed tracking in radar, wireless networks, and satellite communication.

In the subsequent subsection, we will delve into the theory and analysis of the MBPA architecture (Figure 4.1). We'll explore the 90-hybrid, define the planar antenna array, and derive equations for the dual-beam far-field pattern. Additionally, we'll address the grating lobe issue, investigating methods like subarray shifting to eliminate it. The optimization of the shift method for grating lobe cancellation and the calculation of normalized patterns for 8×8 and 64×64 arrays using MATLAB will be discussed.

4.2.1 Dual-beam principle based on 90-hybrid

Figure 4.1 depicts the beam-forming panel in a phased array system comprising N panels feeding N columns of an antenna array in the X direction. Each column has M antenna elements stimulated by a beam-forming panel with M phase shifters and $M/2$ 90-Hybrids. This architecture, shown in Figure 4.1, forms an $M \times N$ antenna array by cascading simplified two-antenna elements illustrated in Figure 4.2.

The building block in Figure 4.2 consists of a 90-hybrid coupler with coupling coefficient C and transmission coefficient T, feeding two antenna elements with a 90-degree phase difference in the X direction. This allows them to act as a sub-array within the $M \times N$ structure. The coupler controls the phase of I and Q signals using conventional phase shifters. Exciting $Port1$ results in a $Right$ beam, and $Port2$ results in a $Left$ beam. The isolation between input ports ensures no coupling of the dual-beam received signals. The TR module of each antenna element observes quadrature phases, enhancing efficiency compared to using a power divider.

The same principle extends to Figure 4.1, where odd-numbered phase shifters fed by $Port1$ control a $Right$ beam, and even-numbered fed by $Port2$ control a $Left$ beam. The $Right$ beam scans the elevation plane along the X axis, and the $Left$ beam scans from $\theta = 0°$ to $\theta = -90°$. Both beams can ideally scan the azimuth plane along the Y axis from $\theta = -90°$ to $\theta = +90°$ simultaneously. The 90-hybrid property enables independent scanning in the elevation plane for $Right$ and $Left$ beams.

4.2.2 Antenna Array Geometry, Amplitude, Phase, and Pattern

The geometry of the $M \times N$ antenna arrays utilized in the phased architecture is depicted in Figure 4.3. These arrays consist of N columns along the Y-axis direction, where each column contains M antenna elements. Each pair of antenna elements that are fed by their corresponding 90-hybrid located behind them serves as a sub-array within the topology of the antenna arrays. The separation distance between the elements along the X direction and the Y axis is denoted by d_x and d_y, respectively. Furthermore, the distance between the two-element sub-array is represented

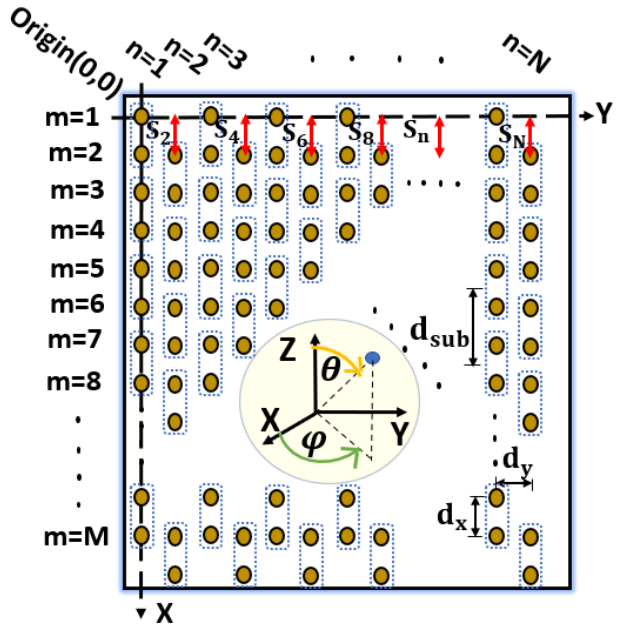

Figure 4.3: $M \times N$ antenna arrays used in phased array architecture.

by d_{sub}. Each column of antenna arrays is shifted along the X direction by a distance of S_i. The location of each element in the planar $M \times N$ array is determined by its distance from the elements in the X and Y axis, as well as the column shift along the X direction is denoted as:

$$\begin{aligned} X_a(m,n) &= (n-1)\, d_x + S_i, \\ Y_a(m,n) &= (m-1)\, d_y, \end{aligned} \tag{4.1}$$

where the variable m with a range of 1 to M is utilized to indicate the index of antenna elements along the X axis, while n ranging from 1 to N represents the antenna element index along the Y axis. Additionally, i ranging from 1 to N signifies the column index shift along the X axis in the $M \times N$ antenna arrays matrix. The presence of a 90-hybrid within the beam-forming panel results in a consistent quadrature phase shift for both the right and left beams, with a 90-degree orthogonality that is represented by the notation $\phi_H^{L/R}(m,n)$:

$$\phi_H^R(m,n) = \begin{cases} \pi/2, & \text{if } m \textit{ is odd.} \\ 0, & \text{otherwise.} \end{cases} \tag{4.2}$$

$$\phi_H^L(m,n) = \begin{cases} \pi/2, & \text{if } m \; is \; even. \\ 0, & \text{otherwise.} \end{cases} \tag{4.3}$$

The phase shifters apply a progressive relative phase shift between antenna elements, which enables the steering of the antenna array's left and right beams towards the specific point θ_0 and ϕ_0 at a given frequency f_0. This phase shift is expressed mathematically in equation (4.4). By applying the progressive phase shift in the phase shifters, the right and left beam radiation pattern are calculated by (4.5).

$$\phi_{ps}^{L/R}(m,n) = -\frac{j2\pi}{\lambda_0} X_a(m,n)u_0 - \frac{j2\pi}{\lambda_0} Y_a(m,n)v_0 ... \\ + \phi_H^{L/R}(m,n), \tag{4.4}$$

by the following:

$$F^{L/R}(\theta,\phi) = f(\theta,\phi) \times \sum_{m,n} |a^{L/R}(m,n)| \times ... \\ e^{[\frac{j2\pi}{\lambda_0} X_a(m,n)(u-u_0) + \frac{j2\pi}{\lambda_0} Y_a(m,n)(v-v_0) + \phi_H^{L/R}(m,n)]}, \tag{4.5}$$

The element factor or single antenna element radiation pattern is represented by $f(\theta,\phi)$, and the variables n and m are within the range of $1, 2, .., N, M$. The tapered amplitude for each element is shown by $a^{L/R}(m,n)$. The space angular factor for the array along the x-coordinate and y-coordinate are respectively denoted as $u = sin(\theta)cos(\phi)$ and $v = sin(\theta)sin(\phi)$. Additionally, $u_0 = sin(\theta_0)cos(\phi_0)$ and $v_0 = sin(\theta_0)sin(\phi_0)$ represent the space angular factor at the desired angles. Ideally, the pointing angle of the $Right$ beam should vary from $\theta_0 = 0^\circ$ to $\theta = 90^\circ$, while the pointing angle of the $Left$ beam should vary from $\theta_0 = 0^\circ$ to $\theta_0 = -90^\circ$. Along the Y axis, both the $Right$ and $Left$ pointing angles should ideally vary from $\theta = -90^\circ$ to $\theta = +90^\circ$.

4.2.3 Grating Lobe Cancellation

The antenna array geometry is extensively covered in 4.2.2, with element separations (d_x and d_y) set to $\lambda_0/2$ at the central frequency f_0 for maximum gain and scanning angle, ensuring antenna

input matching. In 4.2.1 and 4.2.2, pairs of antenna elements in the X direction, fed by a 90-hybrid, act as sub-arrays within the $M \times N$ structure (Figure 4.1 and Figure 4.3). The $\lambda_0/2$ distance between elements results in λ_0 between sub-arrays in Figure 4.3, causing grating lobes shown in Figure 4.4-4.5 for 8 and 32×32 patch antenna elements with zero column shifts (S_i).

Grating lobes, undesirable beams generated in antenna arrays due to large element separations relative to the wavelength, pose challenges like reduced performance, ambiguity in angles, interference, decreased gain, and limited scanning range. In large arrays with low density or a small number of elements, grating lobes are more pronounced, necessitating careful array design for mitigation.

Various methods are proposed in the literature to address grating lobes, such as optimal element shaping [64], numerical optimization techniques (e.g., PSO, GA, least square) [65]-[66], and sub-array distortion [67]. Optimal shaping can reduce grating lobes but at the cost of bandwidth and gain. Numerical optimization techniques optimize array geometry but may complicate feeding networks. Sub-array distortion requires large sub-arrays and complicates feeding networks.

To counter grating lobes in this chapter, antenna array columns are shifted to reduce the gap between sub-arrays virtually along the X axis. Optimal column shifts (S_i) are discussed in 4.2.4 to minimize grating lobes, reduce side-lobe levels (SLL), and maintain maximum antenna matching bandwidth.

4.2.4 Optimal Dual-Beam Phased Array Geometry

In 4.2.1-B-C, two antenna elements in the X direction, fed by a 90-degree hybrid, act as a single sub-array with $\lambda_0/2$ element separation. This causes grating lobes in Figure 4.3 when element spacing exceeds a critical dimension. To address this, a triangular lattice arrangement with optimized column displacements S_i is chosen. For odd $n = 1, 3, ...$, S_i is zero; for even $n = 2, 4, ...$, it's optimized to minimize grating lobes and Side-lobe Level (SLL) while maintaining maximum matching bandwidth.

Details on antenna geometry, progressive phase shift, and radiation pattern derivation are in

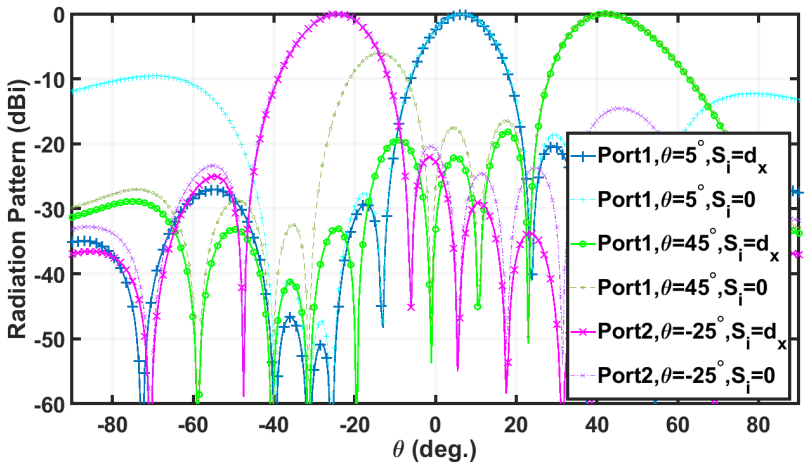

Figure 4.4: Radiation pattern for the proposed dual-beam phased array with $8 * 8$ patch antenna elements, simulated using Matlab software.

4.2.2 and equations (4.1)-(4.5). The relative phase shift for steering right and left beams (θ_0, ϕ_0) depends on element location $(X_a(m,n), Y_a(m,n))$ in (4.4). Right and left beam patterns hinge on element factor, amplitude tapering, phase, and location. Element location is a function of d_x, d_y, and S_i defined by (4.1). To reduce grating lobes and maximize gain, an optimization algorithm, employing Matlab's random search, determines optimal element separations. This process involves sweeping through d_x, d_y, and S_i values to find the ideal displacement for suppressing grating lobes at various steering angles (θ_0, ϕ_0), while maintaining desired gain levels.

For studying input matching, S-parameter, and axial ratio of the optimized antenna array geometry, Ansys-HFSS full-wave simulation uses the best dual-beam phased array performance with gain, bandwidth, and axial ratio. Based on Matlab and HFSS simulations, the best displacement geometry is the triangular grid with $d_x = d_y = S_i = \lambda_0/2$.

To verify the optimum array geometry, two planar arrays with 8×8 and 32×32 elements are optimized to cancel the grating lobe at a center frequency of 12 GHz. The Matlab-calculated radiation pattern for various steering angles of the right and left beams are shown in Figure 4.4 and Figure 4.5. The grating lobe appears when the column shift $S_i = 0$ for various steering angles of the right and left beam. By selecting the column shift equal to the distance between the elements in the X direction ($d_x = S_i$), the grating is canceled for various steering angles of the right and left

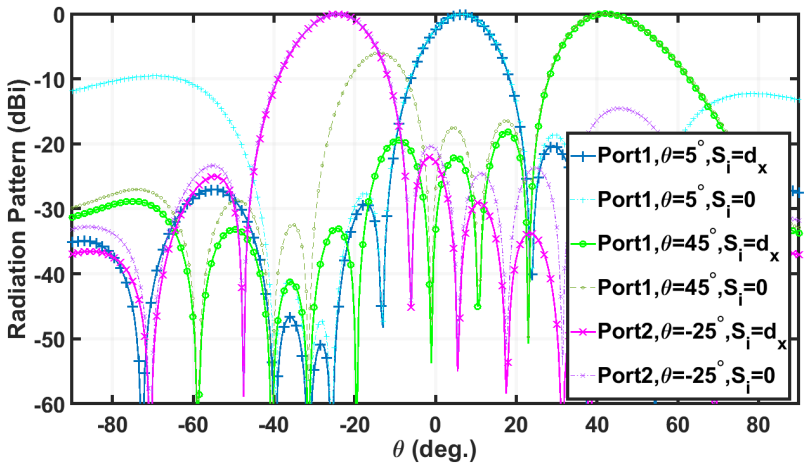

Figure 4.5: Radiation pattern for the proposed dual-beam phased array with 32×32 patch antenna elements, simulated using Matlab software.

beam. After comparing the radiation pattern results of the 8×8 and 32×32 antenna arrays, it can be concluded that the proposed dual-beam phased array architecture is effective for larger arrays with a wider scanning range.

4.3 Dual-Beam Phased Array Design, Simulation, and Measurement

To validate the proposed architecture, an 8×8 phased array with 64 slot-coupled patch antenna elements is fabricated, modeled, and evaluated, as shown in Figure 4.6. The array comprises eight columns along the X-axis, each with four sub-arrays. Each sub-array, consisting of two slot-coupled patch antenna elements, is excited using a single 90-degree hybrid implemented with a two-section branch line coupler on a single-layer PCB. One-to-four power dividers separately sum the left and right beams, applying amplitude tapering. The $ADAR1000$ evaluation board serves as the beamformer for phase shift. Measurement is conducted in an antenna chamber, with the array components mounted on a rack and connected via RF cables.

In Section 4.3.1, detailed discussions cover slot-coupled patch antenna arrays, emphasizing design, fabrication, and optimization. Sub-array architecture is explored, focusing on antenna element placement, orientation, and overall beam-forming capabilities. Section 4.3.2 provides a comprehensive description of the 90-degree hybrid, power divider, and $ADAR1000$ evaluation

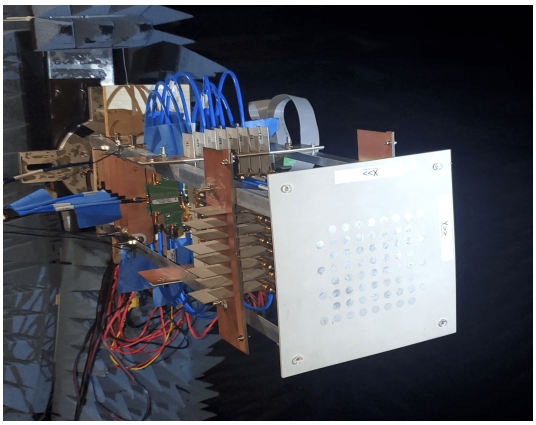

Figure 4.6: Dual-beam 8×8 phased array fabricated prototype.

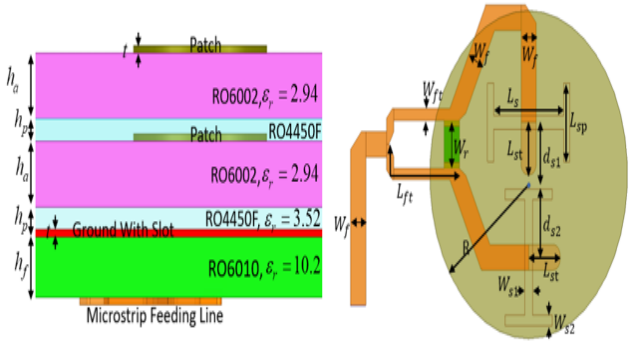

Figure 4.7: Proposed circular polarized patch antenna element.

board, highlighting design features and operational principles. Finally, in Section 4.3.3, results of far-field simulation and measurement are presented and analyzed, comparing simulated and measured performance. The proposed phased array demonstrates excellent performance, suitable for diverse applications like wireless communication, radar, and sensing.

4.3.1 Slot-Coupled Patch Antenna Array

In the realm of satellite communication systems, there has been significant research on high-performance wide-band circular polarized antennas [68]-[69]. This chapter introduces a four-layer antenna design, featuring two metal layers for circular patches resonating at a central frequency f_o, H-shaped slots on the third metal layer for power coupling, and microstrip feedlines on the fourth metal layer connected to a Wilkinson power divider. The antenna substrate is RT Duriod

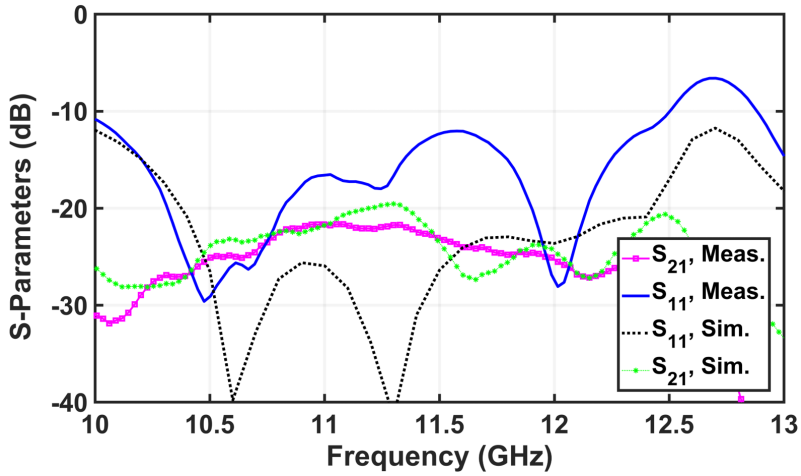

Figure 4.8: The measurement and simulation S-parameter of the patch antenna array.

Table 4.1: Final optimized dimensions of slot coupled patch antenna

R_a	3.77 mm	L_s	2.9 mm
L_{sp}	1.8 mm	L_{st}	1.2 mm
L_{ft}	3.3 mm	W_{s1}	0.3 mm
W_{s2}	0.24 mm	W_f	0.58 mm
W_{ft}	0.27 mm	W_r	1.1 mm
d_{s1}	1.2 mm	d_{s2}	1.9 mm

6002, and the feeding substrate is RT Duriod 6010, chosen to reduce back-radiation and minimize slot size. Two H-shaped slots excite orthogonal modes with equal amplitude and a 90° phase difference for circular polarization. The MSL beneath one slot arm excites the first linear mode, and the other arm excites the second orthogonal mode. The operating frequency and polarization sense are determined by slot arm lengths and MSL location. The design parameters are outlined in Figure 4.7. The antenna design process involves analyzing requirements, determining specifications, designing the patch antenna using analytical formulations, and optimizing the slot coupled feed and antenna structure. Lastly, the Wilkinson power divider feeding network is designed on the selected substrates.

Circularly polarized antennas emit or receive fields with a phase difference of ±90 degrees between the horizontal and vertical radiation field components, with equal amplitudes. The positive or negative phase shift determines the direction of rotation, i.e., counterclockwise (CCW or RHCP

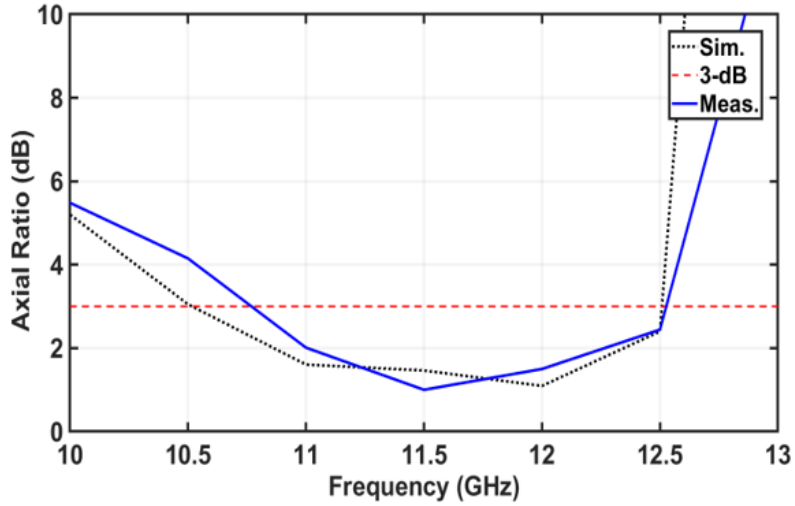

Figure 4.9: Slot-coupled patch antenna axial ratio at bore-sight versus the frequency.

– Right Hand Circular Polarization) or clockwise (CW or LHCP – Left Hand Circular Polarization), respectively. To achieve the desired UWB circular polarization, the radiation problem can be divided into two parts: 1) radiating two orthogonal linearly polarized waves, and 2) generating in-phase and quadrature signals over the desired frequency range. By combining the two subsystems, an ultra-wideband circular polarization system can be created.

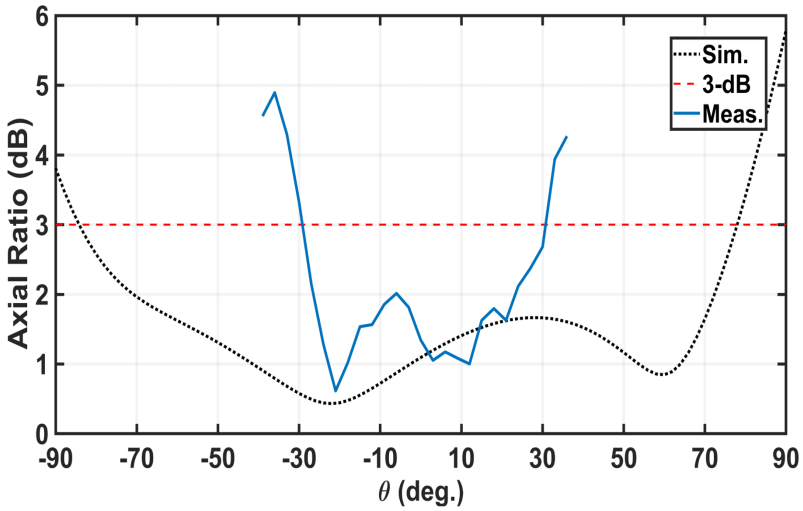

Figure 4.10: Slot-coupled patch antenna axial ratio at 12 GHz versus θ.

Here, two linear H shaped slots, as shown in Figure 4.7, are placed under the radiating patch

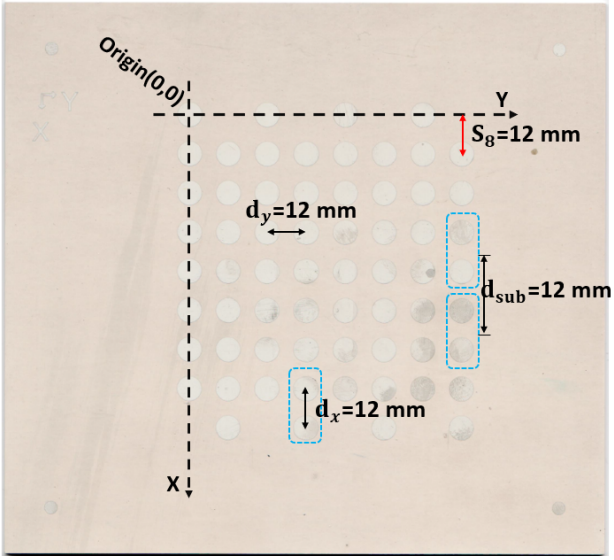

Figure 4.11: Fabricated 8*8 circular polarized patch antenna arrays.

to excite two orthogonal linearly polarized TM_{11} modes on the circular patch with 90° phase difference. The slots are symmetrically oriented about the vertical diameter of the patch. Further, the slots are offset from the center along the same diameter. This arrangement permits the use of resonant lengths of the slots for broadband operation and yet these slots remain almost entirely underneath the patch. This improves slot-patch coupling efficiency and one saves on substrate space.

To achieve a 90° phase difference, the input port of a 90-degree hybrid coupler can be fed, and its output ports can be used to feed the two H shaped slots. By switching the connections between the quadrature hybrid and the H shaped slots, it is possible to switch between LHCP or RHCP operation modes. In this design, a Wilkinson power divider is used, and a 90-degree microstrip transmission line is added to one of the output ports to create I/Q signals that excite the H shaped slots. This design allows the antenna to achieve excellent RHCP circular polarization performance.

Finally, all the design parameters of the antenna are optimized for the operating frequency band, using HFSS full-wave simulator. Final optimized design parameters are given in Table 4.1. The measured and simulated S-parameter of the optimized antenna element are shown in Figure 4.8, show a wide-band S11 over the frequency range 10–12.5 GHz (13.8%). As shown in Figure 4.9, the patch antenna has an $AR < 3\ dB$ over the wide frequency range 10.5–12.5 GHz (12.2%) at

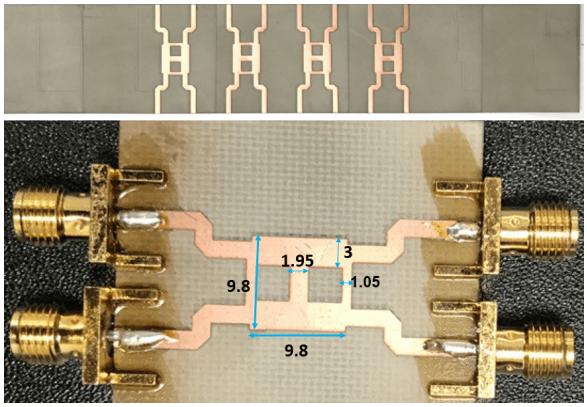

Figure 4.12: The panel of 90-hybrid branch-line coupler, used in phased array architecture. Dimenentions are in mm.

bore-sight direction. Furthermore, the results shown in Figure 4.10 show that the antenna element offers an excellent circular angular beam-width and achieves $AR < 3\ dB$ over $\theta = -30° : +30°$ angular range in elevation at 12 GHz.

The proposed antenna array comprises an 8×8 arrangement of circularly polarized patch antennas, constructed using the geometry shown in Figure 4.3. Multi-layer PCB technology is used to fabricate the antenna array, as depicted in Figure 4.11. Each column of the array contains $M = 8$ antenna elements, with a total of $N = 8$ columns along the X direction. Four sub-arrays are created within each column by pairs of antenna elements that are fed by a relative hybrid located behind them. The separation distances between the antenna elements along the X and Y axes are defined by half wavelength at the center frequency, i.e., $d_x = 12mm$ and $d_y = 12mm$, respectively. The distance between the two-element sub-arrays is $d_{sub} = 24mm$. To suppress grating lobes, each column of the array is shifted along the X direction by a distance of $S_i = d_x = 12mm$, as concluded in section II. To achieve a 90-degree phase shift for circular polarization, a Wilkinson power divider with a 90-degree microstrip transmission line is implemented to excite the H shaped slots. To connect the patch antenna to the feeding layer, a surface mount subminiature push-on (SMP) connector with RF cable is used for each antenna element due to its smaller size compared to the SMA connector, as shown in Figure 4.7 and 4.11.

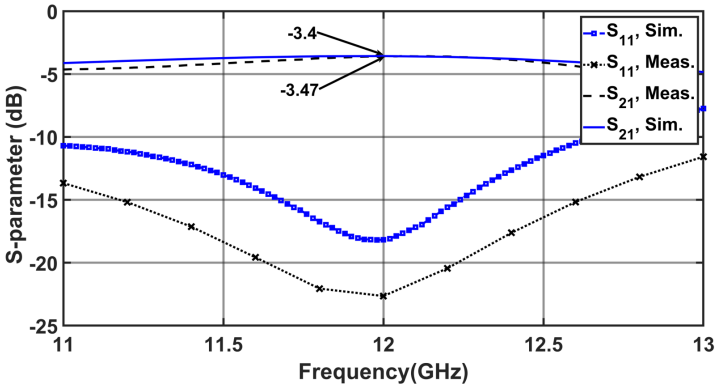

Figure 4.13: Measured and simulated S-parameter of 90-hybrid.

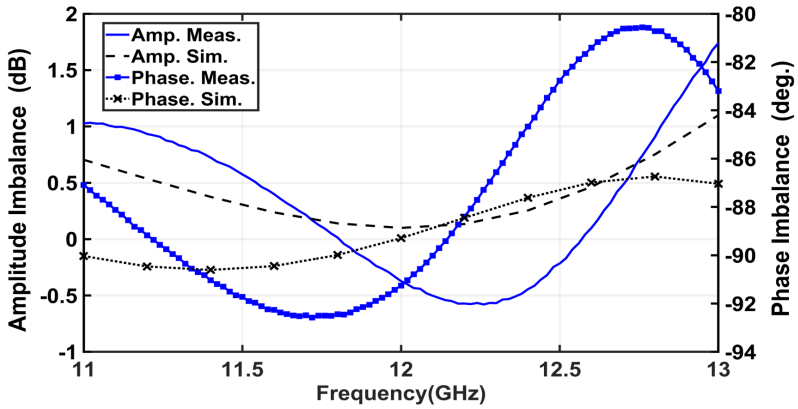

Figure 4.14: Measured and simulated phase and amplitude imbalance of 90-hybrid.

4.3.2 90-Hybrid, Power Divider, and Beamformer Evaluation Board

The 64 elements antenna array arranged in eight columns along the X-axis, with each column consisting of four sub-arrays. which are excited with four 90-degree hybrids. The 90-degree hybrid is implemented using a two-section branch line coupler on a single-layer PCB. The 90-hybrid substrate is RT Duriod 4003 with $\epsilon_r = 3.55$, thickness $h = 0.81mm$, and $\tan\delta = 0.0027$. The designed and fabricated panel of 90-hybrid branch-line coupler is shown in Figure 4.12, including four SMA connctorized 90-hybrids. The SMA to SMP RF cable is used to connect the 90-hybrid and antenna elements.

The design and performance of the coupler are explained in detail in [70] based on even and odd

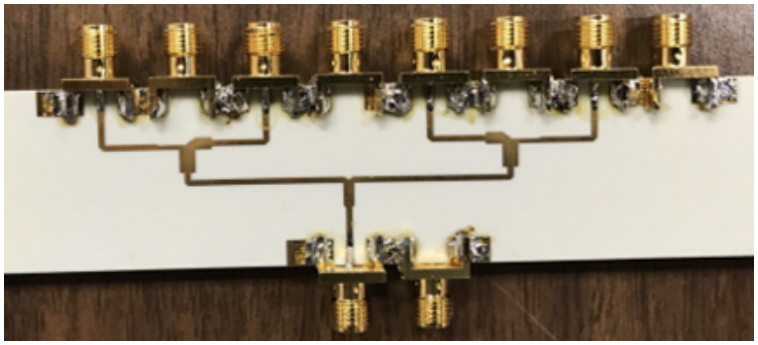

Figure 4.15: Fabricated one-to-four power divider on top and bottom of the substrate.

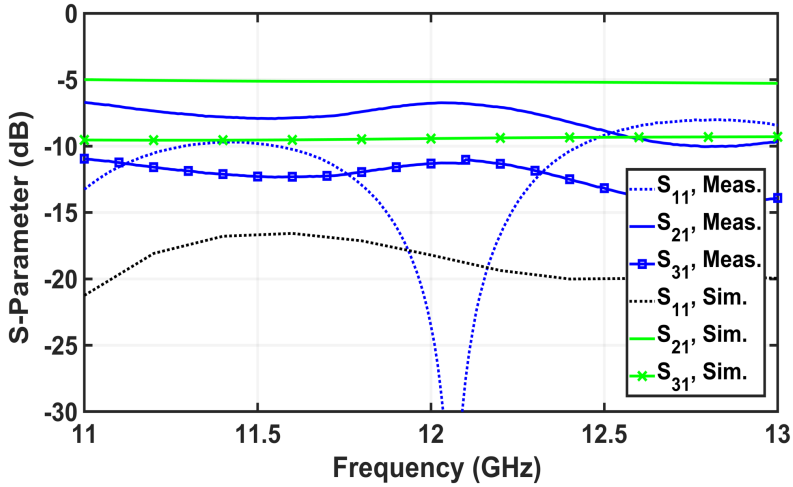

Figure 4.16: Measured and simulated S-parameter of one-to-four power divider.

mode theory. The four port 90-degree hybrid branch-line coupler consists of two quarter-wave parallel coupled lines that are connected with two quarter-wave lines. The performance of a 90-degree hybrid branchline coupler is characterized by several parameters, such as coupling, isolation, phase imbalance, and amplitude imbalance. To have the wider performance for all of these parameters, a two section branch-line coupler is optimized by using Advanced Design System (ADS) software. The measured and simulated S-parameter of the 90-hybrid are shown in Figure 4.13. The S-parameter shows input matching of -10 dB from 11GHz to 13GHz, and -3.47dB coupling plus the insertion loss at 12 GHz. The measured phase and amplitude imbalance are shown Figure 4.14, resulting phase imbalance less than 5 degrees and amplitude imbalance less than 1 dB from 11.5 GHz to 12.5 GHz.

The one-to-four power divider in the phased array demo, depicted in Figure 4.15, is crucial for summing left and right beams from the antenna array. It's designed to apply amplitude tapering between the four sub-arrays, as seen in the power divider S-parameter in Figure 4.16. The design achieved 4 dB amplitude tapering with a difference between S21 and S31.

The ADAR1000 evaluation board, showcased in Figure 4.17, serves as a beam-former for applying phase shifts. Operating in the X and Ku frequency bands, it features four channels for half-duplex operation between receive and transmit modes. In receive mode, input signals combine and output through the common RFIO pin, while in transmit mode, the RFIO input signal is split and passed through four channels. The ADAR1000 provides a 31 dB gain adjustment range, full 360° phase adjustment in each RF channel with 6-bit resolution (2.8° steps), a 4-wire SPI for control, and additional features such as memory for beam positions, power detectors, temperature sensing, an integrated ADC, and programmable bias modes. This evaluation board is well-suited for applications like phased array radar and satellite communications systems.

4.3.3 Simulation and Measurement Result

To assess the performance of the new dual-beam phased array, we constructed an 8 × 8 slot-coupled patch phased array, shown in Figure 4.6. For measuring the 2D steering multiple beams at the central frequency of $12\ GHz$, we employed a broadband standard horn antenna as a feed source. The far-field radiation pattern was detected by the probe, positioned at a distance from the phased array. All height-adjustable devices, including the probe, were digitally controlled using the turntable facility. Once the array was secured on the control turntable, computed height adjustments aligned the central axis of the standard horn antenna and the antenna array, ensuring accurate and reliable measurement of the dual-beam phased array's radiation pattern.

he Figure 4.18 displays the simulated and measured normalized radiation pattern of the demo at the central frequency for azimuth scanning. The phased array scans from $\theta = -35^\circ$ to $\theta = 35^\circ$ in the azimuth plane ($\phi = 90^\circ$), demonstrating excellent agreement between simulation and measurement. Both beams exhibit scanning capability from $\theta = -20^\circ$ to $\theta = +20^\circ$ with a Side-

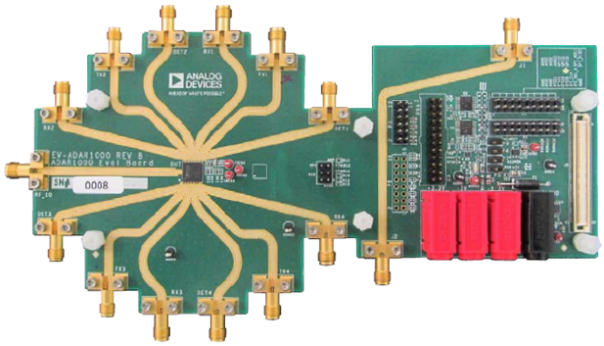

(a) ADAR1000 evaluation board

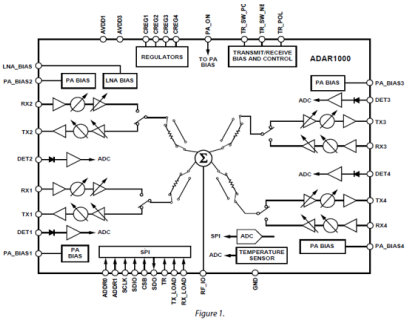

(b) ADAR1000 beam-former architecture

Figure 4.17: The ADAR1000 evaluation board used in the proposed dual-beam phased array demo as a beam-former.

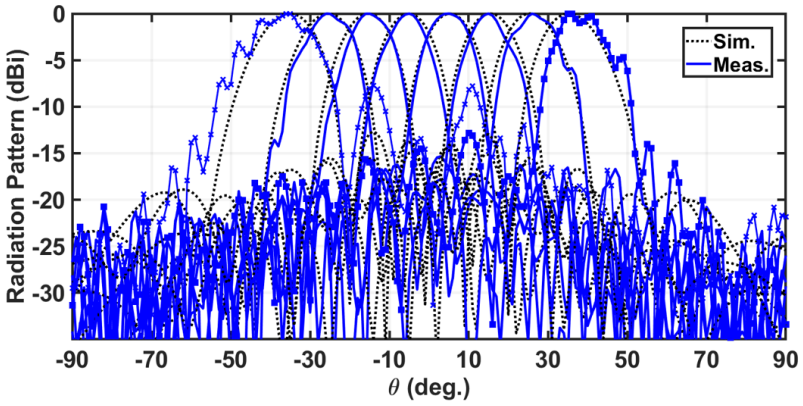

Figure 4.18: The simulated and measured normalized scanning radiation patterns in azimuth plane.

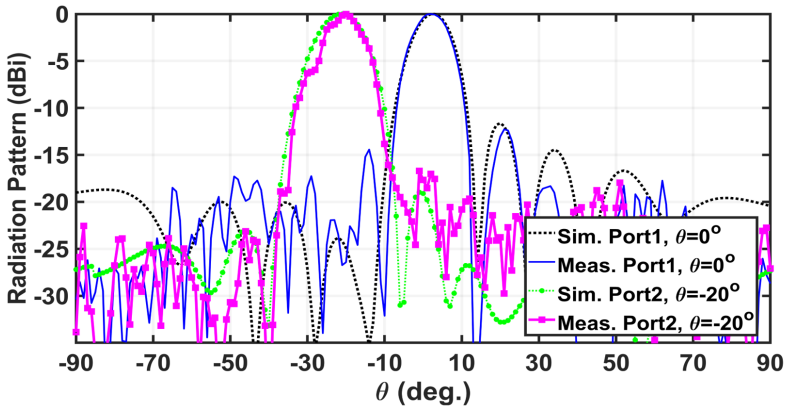

Figure 4.19: The simulated and measured normalized scanning radiation patterns in the elevation plane, when Right beam is directing at $\theta = 0^{\circ}$ and Left beam is directing at $\theta = -20^{\circ}$.

Lobe Level (SLL) less than $-14.3\ dB$.

To further assess the circular-polarized dual-beam phased array antenna, beam scanning is performed in the elevation plane ($\phi = 0^{\circ}$). Independent behavior of the right and left beams is demonstrated through different steering angles, specifically $\theta \in 0^{o}, 10^{o}, 20^{o}, 30^{o}, 45^{o}$. The corresponding simulated and measured normalized radiation patterns at these elevation angles are shown in Figure 4.19, Figure 4.20, and Figure 4.21. Simulation results closely match the measurements, confirming the accuracy and reliability of the proposed dual-beam architecture. The measurement results reveal that the right beam can scan from $\theta = 0^{\circ}$ to $\theta = 45^{\circ}$, and the left beam from $\theta = 0^{\circ}$ to $\theta = -45^{\circ}$, with a Side-Lobe Level (SLL) less than $-13.8\ dB$.

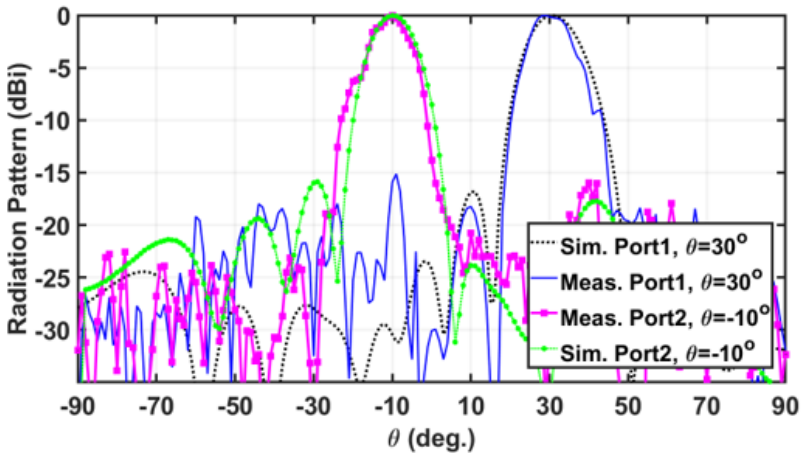

Figure 4.20: The simulated and measured normalized scanning radiation patterns in the elevation plane, when Right beam is directing at $\theta = +30^{\circ}$ and Left beam is directing at $\theta = -10^{\circ}$.

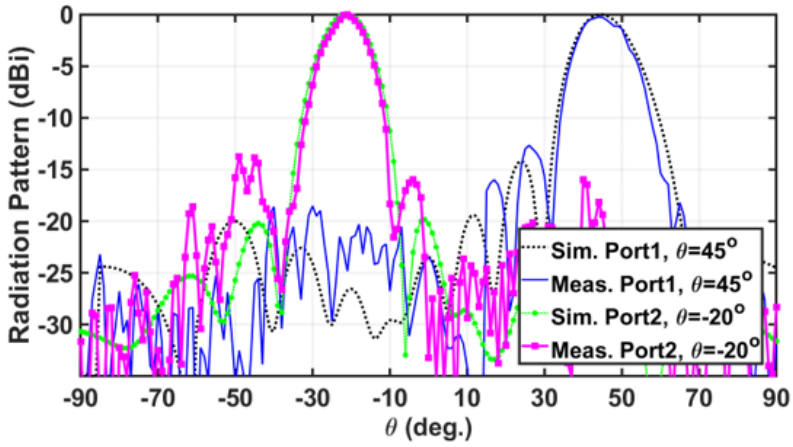

Figure 4.21: The simulated and measured normalized scanning radiation patterns in the elevation plane, when Right beam is directing at $\theta = +45^{\circ}$ and Left beam is directing at $\theta = -20^{\circ}$.

Grating lobes commonly arise in phased arrays, especially during high-angle beam scanning. The proposed architecture, employing a hybrid-90 and orthogonal signal sampling technique, results in significant grating lobes due to large sub-array distances, as shown in Figure 4.4 and Figure 4.5. To address this, optimal column shifts (Si) fill the gap between sub-arrays, virtually reducing the distance along the X axis. Measured normalized radiation patterns for azimuth and elevation planes indicate the absence of grating lobes at scan angles below 20° and 45°, respectively. The optimal column shift method in a triangular lattice effectively eliminates Side-Lobe Level

(SLL). Controlling grating lobes, the proposed phased array achieves a peak gain of $20.8\ dBi$ at $\theta = \pm 21^{\circ}$ in the elevation plane. Unlike conventional phased arrays, this architecture minimizes losses from element patterns during beam scanning, suggesting its potential for diverse wireless and satellite applications.

Chapter 5

CONCLUSION

In conclusion, this dissertation presents novel approaches to design a cost-effective, low-power, low-noise, and highly linear phased array system tailored for commercial wireless applications. The second chapter introduces a new LC-based phase shifter structure to achieve a higher FOM at sub-6 GHz frequencies, vital for 5G applications. This structure utilizes a microstrip transmission line periodically loaded with equivalent capacitance from shunt stubs, with a comprehensive theory developed for design optimization. The resulting phase shifter, designed at 4 GHz, exhibits an impressive FOM of 105.9° /dB and excellent input matching from 3.7 GHz to 4.2 GHz. The measured radiation pattern of the phased array prototype validates the efficacy of the proposed phase shifter, with its planar shape and low-cost fabrication making it a promising candidate for 5G applications.

The third chapter proposes a modified architecture for a mixer-first phased array, achieving a low-noise, robust receiver with superior spatial interference rejection. This architecture employs the novel TVTL MMIC [49] as a mixer, offering high input IP3 (22 dBm) and average noise figure (3 dB). The LO-path utilizes a low-cost LC phase shifter [50] to mitigate the lossy phase shifter's impact on receiver noise figure, consuming zero-DC power and making it an attractive option for commercial applications. Measurement results of the phased array demonstrate continuous beam scanning over the elevation angle of 0° to 20°, confirming the effectiveness of the proposed architecture.

In the fourth chapter, a novel analog beamforming architecture is introduced for a dual-beam 2D-scanning phased array receiver. This design employs a single 90-hybrid block behind each two antenna elements sub-array, with phase shifters at the input ports to generate simultaneous

independent beams. The approach allows for maximum available gain for each beam without dividing the aperture for dual-beams or multiplying the number of phase shifters, making it scalable to larger phased arrays. The demonstration of the dual-beam 2D-scanning phased array showcases wide-band S11 over the frequency range of $10 - 12.5$ GHz and low axial ratio within 3 dB over 10.5-12.5 GHz. The phased array pattern measurement exhibits continuous beam scanning over the elevation angle of 0° to 45° and azimuth angle of 0° to 20° for both right and left beams, with a maximum gain of 20.8 dBi and SLL of -13.7 dB.

REFERENCES

[1] A.-L. Franc, O. H. Karabey, G. Rehder, E. Pistono, R. Jakoby, and P. Ferrari, "Compact and broadband millimeter-wave electrically tunable phase shifter combining slow-wave effect with liquid crystal technology," *IEEE Transactions on Microwave Theory and Techniques*, vol. 61, no. 11, pp. 3905–3915, 2013.

[2] E. A. Firouzjaei, *mm-Wave phase shifters and switches*. University of California, Berkeley, 2010.

[3] R. Amirkhanzadeh, "High resolution integrated passive phase shifters for future wireless communications," Ph.D. dissertation, Victoria University, 2015.

[4] W. Zhu *et al.*, "A 21 to 30 GHz merged digital-controlled high resolution phase shifter-programmable gain amplifier with orthogonal phase and gain control for 5G phase array application," in *2019 IEEE Radio Frequency Integrated Circuits Symposium (RFIC)*, IEEE, 2019, pp. 67–70.

[5] A. Basaligheh, P. Saffari, S. R. Boroujeni, I. Filanovsky, and K. Moez, "A 28–30 GHz CMOS reflection-type phase shifter with full 360 phase shift range," *IEEE Transactions on Circuits and Systems II: Express Briefs*, vol. 67, no. 11, pp. 2452–2456, 2020.

[6] G. McFeetors and M. Okoniewski, "Distributed MEMS analog phase shifter with enhanced tuning," *IEEE Microwave and Wireless Components Letters*, vol. 16, no. 1, pp. 34–36, 2005.

[7] G.-S. Shin *et al.*, "Low insertion loss, compact 4-bit phase shifter in 65 nm CMOS for 5G applications," *IEEE Microwave and Wireless Components Letters*, vol. 26, no. 1, pp. 37–39, 2015.

[8] Z. R. Omam, A. Pourziad, W. M. Abdel-Wahab, S. Nikmehr, S. Gigoyan, and S. Safavi-Naeini, "Two-way tunable phase shifter with arbitrary phase shift ratio at two different frequencies," *IEEE Transactions on Microwave Theory and Techniques*, vol. 68, no. 2, pp. 711–720, 2019.

[9] S. Rangan, T. S. Rappaport, and E. Erkip, "Millimeter-wave cellular wireless networks: Potentials and challenges," *Proceedings of the IEEE*, vol. 102, no. 3, pp. 366–385, 2014.

[10] M. Xiao *et al.*, "Millimeter wave communications for future mobile networks," *IEEE Journal on Selected Areas in Communications*, vol. 35, no. 9, pp. 1909–1935, 2017.

[11] R. Olsen and A. Farstad, "Electromagnetic direction finding experiments for location of trapped miners," *IEEE Transactions on Geoscience Electronics*, vol. 11, no. 4, pp. 178–185, 1973.

[12] A. Giere, P. Scheele, Y. Zheng, and R. Jakoby, "Characterization of the field-dependent permittivity of nonlinear ferroelectric films using tunable coplanar lines," *IEEE Microwave and Wireless Components Letters*, vol. 17, no. 6, pp. 442–444, 2007.

[13] L. M. Blinov, *Structure and properties of liquid crystals*. Springer Science & Business Media, 2010, vol. 123.

[14] F. H. Raab, E. B. Blood, T. O. Steiner, and H. R. Jones, "Magnetic position and orientation tracking system," *IEEE Transactions on Aerospace and Electronic systems*, no. 5, pp. 709–718, 1979.

[15] F. Goelden, S. Mueller, P. Scheele, M. Wittek, and R. Jakoby, "IP3 measurements of liquid crystals at microwave frequencies," in *2006 European Microwave Conference*, IEEE, 2006, pp. 971–974.

[16] M. Nickel *et al.*, "Ridge gap waveguide based liquid crystal phase shifter," *IEEE Access*, vol. 8, pp. 77 833–77 842, 2020.

[17] L. Cai, H. Xu, J. Li, and D. Chu, "High figure-of-merit compact phase shifters based on liquid crystal material for 1–10 GHz applications," *Japanese Journal of Applied Physics*, vol. 56, no. 1, p. 011 701, 2016.

[18] Y Poplavko *et al.*, "Low loss microwave piezo-tunable devices," in *2006 European Microwave Conference*, IEEE, 2006, pp. 657–660.

[19] O. H. Karabey, A. Gaebler, S. Strunck, and R. Jakoby, "A 2-D electronically steered phased-array antenna with 2*2 elements in LC display technology," *IEEE Transactions on Microwave Theory and Techniques*, vol. 60, no. 5, pp. 1297–1306, 2012.

[20] F Goelden, A Gaebler, M Goebel, A Manabe, S Mueller, and R Jakoby, "Tunable liquid crystal phase shifter for microwave frequencies," *Electronics Letters*, vol. 45, no. 13, pp. 686–687, 2009.

[21] S. Bulja, D. Mirshekar-Syahkal, R. James, S. E. Day, and F. A. Fernández, "Measurement of dielectric properties of nematic liquid crystals at millimeter wavelength," *IEEE Transactions on Microwave Theory and Techniques*, vol. 58, no. 12, pp. 3493–3501, 2010.

[22] D.-K. Yang and S.-T. Wu, *Fundamentals of liquid crystal devices*. John Wiley & Sons, 2014.

[23] D. M. Pozar, "Microwave engineering USA: John Wiley & Sons," 2009.

[24] M. J. Rodwell *et al.*, "Active and nonlinear wave propagation devices in ultrafast electronics and optoelectronics," *Proceedings of the IEEE*, vol. 82, no. 7, pp. 1037–1059, 1994.

[25] N. S. Barker and G. M. Rebeiz, "Optimization of distributed MEMS transmission-line phase shifters-U-band and W-band designs," *IEEE Transactions on Microwave Theory and Techniques*, vol. 48, no. 11, pp. 1957–1966, 2000.

[26] M. Himdi, J. Daniel, and C Terret, "Transmission line analysis of aperture-coupled microstrip antenna," *Electronics Letters*, vol. 25, no. 18, pp. 1229–1230, 1989.

[27] C. A. Balanis, *Antenna Theory: Analysis and Design*. John Wiley & Sons, 2015.

[28] C.-S. Lin, S.-F. Chang, and W.-C. Hsiao, "A full-360° reflection-type phase shifter with constant insertion loss," *IEEE Microwave and Wireless Components Letters*, vol. 18, no. 2, pp. 106–108, 2008.

[29] Y. Huang, J. Bao, X. Li, Y. Wang, and Y. Du, "A 4-bit switched-line phase shifter based on MEMS switches," in *10th IEEE International Conference on Nano/Micro Engineered and Molecular Systems*, IEEE, 2015, pp. 405–408.

[30] W. W. Hui, J. M. Bell, M. F. Iskander, and J. Lee, "Low-cost microstrip-line-based ferrite phase shifter design for phased array antenna applications," *IEEE Antennas and Wireless Propagation Letters*, vol. 6, pp. 86–89, 2007.

[31] D. Wang *et al.*, "Fast and miniaturized phase shifter with excellent figure of merit based on liquid crystal and nanowire-filled membrane technologies," *IEEE Journal of Microwaves*, 2021.

[32] H. Tesmer *et al.*, "Feasibility of additively manufactured tunable liquid crystal loaded dielectric waveguides," *IEEE Microwave and Wireless Components Letters*, 2021.

[33] X. Y. Li, D. Jiang, J. Liu, and M. Tong, "A Ka-band multilayer beaming-scanning antenna using liquid crystals," *IEEE Antennas and Wireless Propagation Letters*, 2021.

[34] D. Wang, E. Polat, H. Tesmer, R. Jakoby, and H. Maune, "A compact and fast $1 * 4$ continuously steerable endfire phased-array antenna based on liquid crystal," *IEEE Antennas and Wireless Propagation Letters*, vol. 20, no. 10, pp. 1859–1862, 2021.

[35] D. Parker and D. C. Zimmermann, "Phased arrays-part 1: Theory and architectures," *IEEE transactions on microwave theory and techniques*, vol. 50, no. 3, pp. 678–687, 2002.

[36] D. Ehyaie, "Novel approaches to the design of phased array antennas," Ph.D. dissertation, University of Michigan, 2011.

[37] H. Hashemi, X. Guan, A. Komijani, and A. Hajimiri, "A 24-GHz SiGe phased-array receiver-LO phase-shifting approach," *IEEE Transactions on Microwave Theory and Techniques*, vol. 53, no. 2, pp. 614–626, 2005.

[38] A. Ghaffari, E. A. Klumperink, M. C. Soer, and B. Nauta, "Tunable high-Q N-path band-pass filters: Modeling and verification," *IEEE Journal of Solid-State Circuits*, vol. 46, no. 5, pp. 998–1010, 2011.

[39] A. Mirzaei, H. Darabi, A. Yazdi, Z. Zhou, E. Chang, and P. Suri, "A 65 nm CMOS quad-band SAW-less receiver SoC for GSM/GPRS/EDGE," *IEEE Journal of Solid-State Circuits*, vol. 46, no. 4, pp. 950–964, 2011.

[40] B. van Liempd *et al.*, "A 0.9 v 0.4-6 GHz harmonic recombination SDR receiver in 28 nm CMOS with HR3/HR5 and IIP2 calibration," *IEEE Journal of Solid-State Circuits*, vol. 49, no. 8, pp. 1815–1826, 2014.

[41] L. Duipmans, R. E. Struiksma, E. A. Klumperink, B. Nauta, and F. E. van Vliet, "Analysis of the signal transfer and folding in N-path filters with a series inductance," *IEEE transactions on circuits and systems I: regular papers*, vol. 62, no. 1, pp. 263–272, 2014.

[42] M. H. Kashani, A. Tarkeshdouz, E. Afshari, and S. Mirabbasi, "A 53-67 GHz low-noise mixer-first receiver front-end in 65-nm CMOS," *IEEE Transactions on Circuits and Systems I: Regular Papers*, vol. 66, no. 6, pp. 2051–2063, 2019.

[43] M. Yaghoobi, M. H. Kashani, M. Yavari, and S. Mirabbasi, "A 56-to-66 GHz CMOS low-power phased-array receiver front-end with hybrid phase shifting scheme," *IEEE Transactions on Circuits and Systems I: Regular Papers*, vol. 67, no. 11, pp. 4002–4014, 2020.

[44] G. Pini, D. Manstretta, and R. Castello, "A 260-MHz RF bandwidth mixer-first receiver with third-order current-mode filtering TIA," in *ESSCIRC 2019-IEEE 45th European Solid State Circuits Conference (ESSCIRC)*, IEEE, 2019, pp. 183–186.

[45] S. Qin, Q. Xu, and Y. E. Wang, "Nonreciprocal components with distributedly modulated capacitors," *IEEE Transactions on Microwave Theory and Techniques*, vol. 62, no. 10, pp. 2260–2272, 2014.

[46] M. Hedayati, L. K. Yeung, M. Panahi, X. Zou, and Y. E. Wang, "Parametric downconverter for mixer-first receiver front ends," *IEEE Transactions on Microwave Theory and Techniques*, vol. 69, no. 5, pp. 2712–2721, 2021.

[47] Q. Wu, X. Zou, S. Qin, and Y. E. Wang, "Frequency translational RF receiver with time varying transmission lines (TVTL)," in *2017 IEEE MTT-S International Microwave Symposium (IMS)*, IEEE, 2017, pp. 1767–1769.

[48] X. Zou, Q. Wu, and Y. E. Wang, "Monolithically integrated parametric mixers with time-varying transmission lines (TVTLs)," *IEEE Transactions on Microwave Theory and Techniques*, vol. 68, no. 10, pp. 4479–4490, 2020.

[49] Q. Wu, X. Zou, and Y. E. Wang, "Monolithically integrated directly pumped time-varying transmission lines," *IEEE Transactions on Microwave Theory and Techniques*, 2022.

[50] M. A. Panahi, L. Yeung, M. Hedayati, and Y. E. Wang, "Sub-6 GHz high FOM liquid crystal phase shifter for phased array antenna," *IEEE Journal of Microwaves*, vol. 2, no. 2, pp. 316–325, 2022.

[51] X. Zou, Q. Wu, and Y. E. Wang, "Monolithically integrated parametric mixers with time-varying transmission lines (TVTLs)," *IEEE Transactions on Microwave Theory and Techniques*, vol. 68, no. 10, pp. 4479–4490, 2020.

[52] S. Qin, Q. Xu, and Y. E. Wang, "Nonreciprocal components with distributedly modulated capacitors," *IEEE Transactions on Microwave Theory and Techniques*, vol. 62, no. 10, pp. 2260–2272, 2014.

[53] L. M. Blinov, *Structure and properties of liquid crystals*. Springer Science & Business Media, 2010, vol. 123.

[54] S. C. Blaakmeer, E. A. Klumperink, D. M. Leenaerts, and B. Nauta, "The blixer, a wideband balun-LNA-I/Q-mixer topology," *IEEE Journal of Solid-State Circuits*, vol. 43, no. 12, pp. 2706–2715, 2008.

[55] B. Guo, H. Wang, and G. Yang, "A wideband merged cmos active mixer exploiting noise cancellation and linearity enhancement," *IEEE Transactions on Microwave Theory and Techniques*, vol. 62, no. 9, pp. 2084–2091, 2014.

[56] S. Qin, Q. Xu, and Y. E. Wang, "Nonreciprocal components with distributedly modulated capacitors," *IEEE Transactions on Microwave Theory and Techniques*, vol. 62, no. 10, pp. 2260–2272, 2014.

[57] Q. Wu, X. Zou, S. Qin, and Y. E. Wang, "Frequency translational RF receiver with time varying transmission lines (TVTL)," in *2017 IEEE MTT-S International Microwave Symposium (IMS)*, IEEE, 2017, pp. 1767–1769.

[58] C. A. Balanis, *Antenna theory: analysis and design*. John wiley & sons, 2015.

[59] S. Liu *et al.*, "Leo satellite constellations for 5G and beyond: How will they reshape vertical domains," *IEEE Communications Magazine*, vol. 59, no. 7, pp. 30–36, 2021.

[60] H. Al-Hraishawi, H. Chougrani, S. Kisseleff, E. Lagunas, and S. Chatzinotas, "A survey on non-geostationary satellite systems: The communication perspective," *IEEE Communications Surveys & Tutorials*, 2022.

[61] L. Yu, J. Wan, K. Zhang, F. Teng, L. Lei, and Y. Liu, "Spaceborne multi-beam phased array antennas for satellite communications," *IEEE Aerospace and Electronic Systems Magazine*, 2022.

[62] V. Singh, A. Prabhakara, D. Zhang, O. Yağan, and S. Kumar, "A community-driven approach to democratize access to satellite ground stations," *GetMobile: Mobile Computing and Communications*, vol. 26, no. 1, pp. 35–38, 2022.

[63] I. Ahmed *et al.*, "A survey on hybrid beamforming techniques in 5G: Architecture and system model perspectives," *IEEE Communications Surveys & Tutorials*, vol. 20, no. 4, pp. 3060–3097, 2018.

[64] F. J. Pompei and S.-C. Wooh, "Phased array element shapes for suppressing grating lobes," *The Journal of the Acoustical Society of America*, vol. 111, no. 5, pp. 2040–2048, 2002.

[65] P. J. Bevelacqua and C. A. Balanis, "Geometry and weight optimization for minimizing sidelobes in wideband planar arrays," *IEEE Transactions on Antennas and Propagation*, vol. 57, no. 4, pp. 1285–1289, 2009.

[66] Y. Liu, X. Huang, K. Da Xu, Z. Song, S. Yang, and Q. H. Liu, "Pattern synthesis of unequally spaced linear arrays including mutual coupling using iterative fft via virtual active element pattern expansion," *IEEE Transactions on Antennas and Propagation*, vol. 65, no. 8, pp. 3950–3958, 2017.

[67] T. J. Brockett and Y. Rahmat-Samii, "Subarray design diagnostics for the suppression of undesirable grating lobes," *IEEE transactions on antennas and propagation*, vol. 60, no. 3, pp. 1373–1380, 2011.

[68] I. Russo, P. F. Freidl, and E. Leitgeb, "Slot-coupled UWB circularly polarized patch antenna with matching reflector," in *Proceedings of the 12th International Conference on Telecommunications*, IEEE, 2013, pp. 179–184.

[69] E.-c. Choi, J. W. Lee, and T.-K. Lee, "Modified s-band satellite antenna with isoflux pattern and circularly polarized wide beamwidth," *IEEE antennas and wireless propagation Letters*, vol. 12, pp. 1319–1322, 2013.

[70] D. M. Pozar, *Microwave engineering*. John wiley & sons, 2011.